arXiv:nucl-ex/0103006v1 15 Mar 2001

Precision Pion–Proton Elastic Differential Cross Sections at Energies Spanning the Δ Resonance

M.M. Pavan[†*], J.T. Brack[‡], F. Duncan[§], A. Feltham[**], G. Jones, J. Lange[††], K.J. Raywood[*], M.E. Sevior[‡‡]
Department of Physics, University of British Columbia, Vancouver, British Columbia V6T-1Z1

R. Adams, D.F. Ottewell, G.R. Smith[***], B. Wells, R.L. Helmer
TRIUMF, Vancouver, British Columbia V6T-2A3

E.L. Mathie, R. Tacik
University of Regina, Regina, Saskatchewan S4S-0A2

R.A. Ristinen
Department of Physics, University of Colorado, Boulder, Colorado 80309

I.I. Strakovsky[†††]
Petersburg Nuclear Physics Institute, Gatchina, St. Petersburg, Russia, 188350

H-M. Staudenmaier
Institute for Theoretical Particle Physics, University of Karlsruhe, Karlsruhe D-76128, Germany
(February 8, 2008)

A precision measurement of absolute $\pi^{\pm}p$ elastic differential cross sections at incident pion laboratory kinetic energies from T_π = 141.15 to 267.3 MeV is described. Data were obtained detecting the scattered pion and recoil proton in coincidence at 12 laboratory pion angles from 55° to 155° for π^+p , and six angles from 60^0 to 155^0 for π^-p. Single arm measurements were also obtained for π^+p energies up to 218.1 MeV, with the scattered π^+ detected at six angles from 20^0 to 70^0. A flat–walled, super-cooled liquid hydrogen target as well as solid CH_2 targets were used. The data are characterized by small uncertainties, ∼1-2% statistical and ∼1-1.5% normalization. The reliability of the cross section results was ensured by carrying out the measurements under a variety of experimental conditions to identify and quantify the sources of instrumental uncertainty. Our lowest and highest energy data are consistent with overlapping results from TRIUMF and LAMPF. In general, the Virginia Polytechnic Institute SM95 partial wave analysis solution describes our data well, but the older Karlsruhe–Helsinki PWA solution KH80 does not.

25.90.Dj,13.75.Gx,21.45.+v,25.10.+s

[†]Corresponding Author: e-mail - marcello.pavan@triumf.ca
[*]Present address: TRIUMF, Vancouver, British Columbia V6T 2A3
[‡]Present address: Department of Physics, University of Colorado, Boulder, Colorado 80309
[§]Present address: Department of Physics, Queen's University, Kingston, Ontario K7L 3N6
[**]Present address: Broadcom Canada Ltd. Richmond, British Columbia V6V 2Z8
[††]Present address: Defense Research Establishment, Ottawa, Ontario K1A 0Z4
[‡‡]Present address: School of Physics, University of Melbourne, Parkville, Victoria 3052, Australia
[***]Present address: Jefferson Lab, 12000 Jefferson Avenue, MS 12H Newport News, Virginia 23606
[†††]Present address: Center for Nuclear Studies and Department of Physics, The George Washington University, Washington, DC 20052

I. INTRODUCTION

The pion-nucleon (πN) system at energies up to the first (Δ) resonance continues to be an area of keen theoretical and experimental interest. This is due in large part to the intimate connection of low energy πN scattering to SU(2) quantum chromodynamics (QCD) at low energies. By studying the low energy interactions of pions and nucleons, one is able to probe the confinement scale structure of QCD (via an effective theory, chiral perturbation theory, or ChPT [1,2]). Two key areas of interest in low energy πN QCD centre on determinations of the precise values of the πN sigma term Σ [3–5] and the πNN coupling constant $f^2_{\pi NN}$ [3,6]. The πN sigma term is fundamental to low energy QCD since it quantifies the explicit breaking of chiral symmetry due to the non-zero up and down quark masses. The coupling constant f^2 is *the* fundamental free parameter in ChPT involving nucleons [7]. It also appears in the well-known Goldberger–Treiman relation [8,9], which relates f^2 to the accurately known pion decay constant F_π, nucleon mass M, and axial-vector coupling constant, g_A. The analogous Dashen-Weinstein sum rule [9–11] relates f^2 to coupling constants involving kaons, sigma and lambda baryons, and is closely connected to the quark condensate $\overline{q}q$ [12,13].

Despite many years of investigation, there is still no broad consensus regarding the precise values of these important quantities. The "sigma term puzzle" [14] refers to the historical discrepancy between the phenomenologically determined value [15] and the theoretical prediction [16], a discrepancy which could imply a large strange quark content of the proton. The puzzle has yet to be resolved [3,5]. The value of the coupling constant f^2 has been controversial as well [6], with recent results split roughly into two groups: $f^2 \sim 0.0795$ [17,18] and 0.0755 [6,19,20]. The $\sim$5% difference has significant implications for the aforementioned Goldberger-Treiman and Dashen-Weinstein relations, as well as for any model employing the πNN vertex (e.g. the Bonn NN potential [21,22]).

A major reason for the difficulty in determining Σ and f^2 arises from historical incompatibilities in the πN scattering database [23]. As the determination of these parameters requires extrapolations of the scattering amplitudes to nonphysical kinematic points, an internally consistent database of precision data is crucial for reliable results. The most trustworthy analyses employ πN dispersion relations [24]. Since the P_{33} πN partial wave amplitude in the delta resonance (Δ) region dominates the dispersion relations used to obtain Σ and f^2 [24], it is crucial that the data in this energy region be reliable, mutually consistent, and of high quality. Differential cross section data are of particular importance, yet to date only one comprehensive data set exists spanning the Δ resonance[1], the work of Bussey et al. [26]. Unfortunately, the Bussey data, and that of the companion total cross section work of Carter et al. [27], are generally at variance with partial-wave analyses [19,20] based on recent differential cross section data below 140 MeV kinetic energy [28,29] and above 267 MeV [30], as well as with the other total cross section data of Pedroni et al. [31] across the resonance (Fig. 1). Moreover, the normalization uncertainties in the Bussey et al. data recently have been increased *post priori* [32], indicating possible problems with the data, thus making a new measurement all the more relevant and important.

The goal of the work described in this paper was to provide a new comprehensive set of precision $\pi^\pm p$ absolute differential cross section data characterized by reliable estimates of systematic uncertainties at energies spanning the Δ resonance. Experimental details such as the apparatus, the data acquisition system, and the data-taking techniques are described in Sec. II. The offline data analysis and the Monte Carlo simulations are detailed in Sec. III, and the results are presented in Sec. IV, followed by a discussion in Sec. V. Additional details can be found elsewhere [33].

II. EXPERIMENT

The experiment was conducted on the M11 pion channel at TRIUMF. Data were obtained for both π^+p and π^-p elastic scattering at incident pion lab kinetic energies of $T_\pi = 141.15\pm0.6, 168.8\pm0.7, 193.2\pm0.7, 218.1\pm0.8, 240.9\pm0.9$, and 267.3 ± 0.9 MeV, and for π^+p, at 154.6 ± 0.6 MeV as well. These energies were chosen to span the Δ resonance, to overlap the highest energy used by Brack et al. [28] and the lowest of Sadler et al. [30], and to coincide with those of the $\pi^\pm$p analyzing power measurements of Sevior et al. [34] since the availability of both differential cross sections and analyzing powers at the same energies facilitates single-energy partial wave analyses. For all energies, $\pi^\pm$p two–arm coincidence data were obtained at middle and near-backward angles, while single-arm results (with only the scattered π^+ detected) were obtained at near–forward angles at 141.15, 168.8, and 218.1 MeV.

Although the main goal of the experiment was to obtain statistically precise results, a study of the various sources of systematic uncertainty was also an important feature of this work. As pointed out by Bugg [35], the six elements essential to a measurement of absolute differential cross sections are accurate knowledge of the: 1) beam intensity, 2)

[1]Other data sets exists in this region, e.g. [25], but the data are much more limited in number.

beam composition, 3) beam momentum, 4) target thickness, 5) solid angles, and 6) backgrounds. To ensure confidence in the results, the uncertainties claimed for the measurements should be based on the extent to which the values at each fixed kinematical point are independent of measured variations in the experimental conditions. In this way systematic uncertainties can be more accurately and reliably determined.

The general layout of the experiment is illustrated in Fig. 2. A complete description of the detector elements is presented in the following sections.

A. Pion Beam

For our experiment, the pion beam originated at a beryllium target in the 140 μA primary proton line, BL1A, which yields a proton beam consisting of pulses ∼3-4 ns wide occurring with a repetition rate of 23.06 MHz. After momentum selection in the M11 pion channel, the pions were brought to a doubly-achromatic double-focus at the target location.

The incoming pion beam was detected by three beam-defining scintillators (S1, S2A, S2B) operating in three-fold coincidence and placed upstream of the target. All consisted of 1.59 mm thick NE110, wrapped by a single layer of 0.025 mm aluminum foil and 0.263 mm electrical tape. These counters were connected by short straight lucite light guides to photomultiplier tubes mounted on high-rate transistorized bases [36]. Alignment of the counters was carried out using an optical transit. The 25.4 mm wide by 102 mm high S1 counter was placed 903 mm upstream[2] of the target centre, and 187 mm from the exit of the 200 mm diameter M11 beam pipe. The 12.7 mm wide by 44.5 mm high S2A and S2B counters were placed 410 and 405 mm, respectively, upstream of the target location. They were mounted so that the S2A phototube was above the scintillator and the S2B phototube below. This ensures that muons from pion decay downstream of S1 would not cause erroneous coincidences by producing Čerenkov light in a S2 light guide that could be detected by the phototube, since such muons could hit only one of the two S2 light guides, and so such events were eliminated by the coincidence requirement. Although the exact spot sizes depended on the settings of the rate-defining aperture (jaws) at the front end of the channel, the beam distributions at the target were typically 10 x 8 mm^2 and 1^0 x 4^0 at half-maximum.

Two counter telescopes, each with two scintillators in coincidence, were used to monitor beam intensity relative to the beam counters. One set above the M11 beam pipe exit was used to detect muons from pion decay in the channel. The other set was mounted at beam height in the experimental area and oriented to view particles back-scattered from the S2A,B counters.

To determine the fraction of beam bursts containing only one pion (see Sec. III B 5), it was necessary to know the full beam rate on target, which was somewhat larger than the rate measured by the beam counters. For this purpose, a 201 x 201 x 6.35 mm^3 VETO paddle was placed 1230 mm downstream of the target position. This counter intercepted >95% of the incoming pion beam.

Each beam counter signal was electronically fanned–out and fed to a constant–fraction–discriminator (CFD). The counter voltages and CFD thresholds were set so that all minimum ionizing particles were detected but the thermionic tube noise was not. A second signal from the S2B counter was fed to a leading-edge discriminator in which the threshold was set to detect only very large pulse height signals (S2BH), corresponding to the proton contamination in the incident beam during π^+ running. Inversion of the S2BH output ($\overline{\text{S2BH}}$) thus indicated a "no–proton" event. Use of this signal together with a differential absorber at the channel mid-plane reduced proton contamination in the beam definition to <0.1%.

An incident particle was identified electronically by the four–fold coincidence BEAM $\equiv$ S1 $\cdot$ S2A $\cdot$ S2B $\cdot$ $\overline{\text{S2BH}}$. The logic signal S2B defined the timing for the entire system. The tight angular definition of this telescope of beam counters ensured that all BEAM coincidences corresponded to a particle at the target (except for those pions which decayed or suffered hadronic interaction prior to reaching the target, as described in Sec. III B 4). Particle identification (see Sec. III B 2) was realized by measuring the relative times-of-flight (TOF) of the particles down the pion channel, values obtained from the time differences between the BEAM coincidence and the TCAP signal, the latter a signal produced by a capacitive pickup in the primary proton beam line.

In order to monitor the incident beam, a special "beam samples" trigger (SAMPLE) was constructed which utilized only BEAM coincidences selected randomly by an adjustable clock pulse. Since the vast majority of BEAM triggers did not cause πp events, this trigger provided an unbiased sample of events striking the beam counters.

[2]All distances are between centres, unless otherwise stated

In order to assess the fraction of BEAM coincidences consisting of more than one pion, pions detected in the two buckets following the one that triggered the spectrometer were also monitored. Circuits were constructed to detect BEAM hits in 2 and 3 consecutive beam buckets after an initial BEAM event. According to Poisson statistics, the probability of at least one hit occurring in each of 'm' consecutive beam buckets is $(1 - e^{-\lambda})^m$, where λ is the probability of a pion occurring in a single beam bucket. This relationship was found to be well reproduced throughout the experiment. As discussed in Sec. III B 5, such information was required to correct the beam rate for those events characterized by more than one pion in a beam bucket.

For all of our π^+ measurements, the channel slit width was set at 18 mm, corresponding to a 1% FWHM δp/p momentum spread [37]. For the π^- runs where the fluxes were lower, the momentum spread was set at 2%, except for 267 MeV, where it was 2.5%. The channel jaws were adjusted at each energy to provide typically 1.5MHz and 2MHz target rates for π^+ and π^-, respectively.

A comprehensive beam tuning and calibration program [33] was undertaken immediately prior to the experiment in order to gain a detailed understanding of the pion beam characteristics. Two issues which arose from those studies deserve particular mention. The spot size and divergence of the beam at our target location were found to vary slightly with the aperture of the front–end rate restricting jaws in the channel. Consequently, the values of the jaw apertures were recorded for all data-taking runs, since knowledge of the beam size and divergence was required for accurate modelling by the Monte Carlo simulation programs (see Sec. III and and Appendix A). It was also found that although the pion beam trajectory and size were rather insensitive to the horizontal position of the primary proton beam on the beryllium pion production target, they were somewhat sensitive to the vertical position. To monitor beam movement, a square, four-paddle hodoscope centred on the beam was placed 2480 mm downstream of the target location. The rate on each hodoscope paddle was continuously monitored and written to the data acquisition stream throughout the experiment.

1. Beam Momentum

As the central pion momentum transmitted by the channel is linearly related to the magnetic field strength of the first channel dipole (B1) measured by an NMR probe set at the magnet mid-plane, momentum calibrations were carried out during the tuning phase of the experiment and again near its completion, using the traditional technique (SSBD) [38] of stopping light ions produced at the production target in a silicon counter in vacuum at the beam pipe exit. However, after the experiment, we were made aware [39] of a pulse-height defect issue [40–45] which rendered these results unreliable. Consequently, another detailed calibration was performed subsequent to the experiment by measuring pion–electron TOF differences between scintillators contained within an evacuated beam pipe in the experimental area, and also between the TCAP signal from the protons in the primary beam line and a scintillator in the experimental area. The technique exploits the fact that the electrons travel at essentially the speed of light and so provide an absolute velocity scale. Details are provided in Ref. [33]. Data from these measurements (Fig. 3) yielded the M11 channel momentum calibration:

$$\mathrm{P_{M11}[MeV/}c] = 326.7 \cdot (\mathrm{B1} - 0.00171) \pm 0.2\% \tag{1}$$

where B1 is the magnetic field strength in Tesla, and the $\pm 0.2\%$ uncertainty in $\mathrm{P_{M11}}$ corresponds to the spread in the calibration points from the best fit line shown in Fig. 3. The previously-accepted M11 calibration [38] (which employed the SSBD method) is shown in Fig. 3 as well. The $\approx$0.25% discrepancy in momentum between this calibration and the new one is consistent with the size of the pulse-height defect effects discussed in Refs. [40–45][3].

For each run in the experiment, the energy loss through the mid-plane absorber, the beam pipe exit window, and the in–beam counters (including tape), air, target windows, etc. (for the LH_2 target), and half the target material at the appropriate angle were determined using the full Bethe–Bloch equation [46]. The uncertainty in this energy loss was estimated as 10% of the total loss (ΔT_π typically 2 MeV), and was added in quadrature to the $\pm 0.20\%$ momentum uncertainty calibration to give the total uncertainty. Although the pion beam energy was fine-tuned for each different target configuration to give the desired energy at the target centre, the energies were *not* similarly adjusted for the corresponding background runs, since the backgrounds were small as was the energy-dependence of the background itself. The variations in the cross sections associated with the resulting momentum uncertainty are less than about 1.7% for both our π^+p and π^-p data.

[3] As an uncertainty in the M11 calibration of about ± 0.5 MeV was quoted by Brack *et al.* [28] for their differential cross section results at energies up to 140 MeV, their old calibration is within the 0.2% momentum uncertainty of the new one at 140 MeV.

B. Time-of-Flight Spectrometer

The TOF spectrometer shown in Fig. 2 consisted of the beam monitoring scintillators, six arms consisting of pairs of thin scintillation counters to detect the scattered pions, and six conjugate arms of thin scintillation counters to detect the recoil protons during coincidence running. Use of thin transmission scintillators ensured virtually 100% detection efficiency with negligible edge effects for both π^+ and π^- as well as protons[4]. A pion arm consisted of a two–counter telescope viewing the target, with each telescope comprised of two 3.2 mm thick NE102 scintillators wrapped by a single layer of 0.025 mm aluminum foil and 0.26 mm polyvinylchloride electrical tape. The scintillators were attached to the phototubes via lucite light guides. The telescopes were bolted onto a machined table, with both scintillators of each arm positioned using a transit located at the target centre, enabling the angular positions to be known to better than $\pm 0.2^0$. The solid angle defining 'π2' counters were on average 40.03±0.06 mm wide by 99.90±0.09 mm high [47] and were mounted 1231±3 mm from the target centre. The 'π1' counters were 49 mm by 165 mm, and situated 792 mm from the target centre. These dimensions and separations were chosen in order to define a projected spot size of ≈60 mm horizontal, ≈200 mm vertical at the target, large enough to cover the whole interaction region while not severely restricting the acceptance to muons arising from decay of scattered pions.

For those runs involving coincidence detection (πp) of both pions and protons, a set of six 90 mm by 400 mm by 3.2 mm thick ('P1') scintillators were used as the recoil–proton detection arms. These scintillators were viewed from both the top and bottom by phototubes coupled to lucite light guides bent at 90^0 so that the phototubes pointed radially. The scintillators were situated 926±3 mm from the target. The base plates for these counters were positioned also on a machined table using a transit, with slight adjustments provided in order for the proton counters to be moved after every energy change to the angles conjugate to the scattered pions. An accuracy of about $\pm 0.1^0$ was achieved in the angular positions.

1. Two–Arm πp Coincidence Detection

Pions scattered into the pion arms were identified by a $\pi 1 \cdot \pi 2$ coincidence between counters in the same arm, in any one of the six telescopes (i.e. $\Pi_i \equiv \pi 1_i \cdot \pi 2_i$). Phototube voltages and discriminator thresholds were set just above the noise signals and at about 35% of the smallest pion pulses to ensure that no good pion events would be lost. Particles were identified by their TOF to the π2 counters relative to the BEAM signal. Although neither the timing nor pulse height information from π2 could distinguish pions from those muons arising from pion decay between the target and π2, this small muon contribution could be accurately accounted for by Monte Carlo. The π1 counters were positioned such that pions passing through them would not strike the π2 light guide near the phototube junction, which would enable forward–going Čerenkov radiation to be detected, but nevertheless a check was made with the π1 counters out of the EVENT coincidence. In this case the false events produced by the Čerenkov radiation were easily discriminated against with a timing cut, since the the light arising from true events hitting the π2 scintillator counters had a longer path length to traverse before reaching the phototube.

Proton arm events were signalled by a coincidence between the up and down tubes of each of the P1 counters. Logic signals obtained by discriminating with CFDs were then fed to a meantimer to establish the timing gate. Prior to performing the actual experiment, each counter was placed in the beam, and the phototube voltages and discriminator thresholds were adjusted to cut half–way into the (minimum ionizing) electron signal, thus ensuring that all protons were detected. Candidate πp scattering events (ARM) were identified by the coincidence of BEAM with the coincidence output of signals from a pion arm and its conjugate proton arm (i.e., $\mathrm{ARM}_i \equiv \mathrm{BEAM} \cdot \Pi_i \cdot \mathrm{P}_i$). The timing was set such that only relatively fast particles in the pion arm and relatively slow particles in the proton arm would satisfy the $\Pi \cdot$P coincidence.

The πp scattering yield was obtained from the spectra of TOF differences of particles to the pion counters relative to those to the proton counters. The tight geometry of the counter pairs greatly suppressed the dominant 3–body quasi–elastic $\pi^{\pm}\mathrm{A} \rightarrow \pi^{\pm}\mathrm{pX}$ background, and, combined with the timing requirement, also suppressed the quasi–free absorption $\pi^+\mathrm{A} \rightarrow \mathrm{ppX}$ background. These backgrounds for the two–arm coincidence measurements *never* exceeded 7% of the foreground at any angle or energy. Figure 4 shows the yield spectrum for the *worst case*.

With the system set up as described, data were obtained for both π^+ and π^- for the pion lab angles 60, 75, 95, 115, 135, 155 ("set A") at all energies with $\theta_{\mathrm{tgt}} = 53.6°$, and an additional set at 55, 65, 85, 105, 125, 145 ("set B")

[4]The pion detection efficiency of the lucite light guides attached to the scintillators was measured to be negligible.

for a few π^+p energies with $\theta_{\rm tgt} = 50.6°$. The proton angles were adjusted at each beam energy to the appropriate values conjugate to those of the pion arms.

The possibility of an ARM$_i$ coincidence being generated by the detection of a proton in the pion arm and a pion in the proton arm was completely eliminated in all but a single case by the tight kinematical constraints imposed by the pion–proton counter pairs. The one case where such events could occur was in the "Set B" configuration where both the pion and proton angles were $\approx 55^0$. These events were easily separated from the true πp events by the TOF timing difference, and therefore did not present a problem in the analysis.

As shown in Fig. 2, the targets were arranged such that the pion arms faced the upstream surface of the target (with respect to the incident beam), whereas the proton arms faced the downstream surface to minimize proton energy loss and multiple scattering. The target angles were chosen to minimize the target thickness for the lowest energy protons. The requirement that these protons not suffer excessive energy loss and multiple scattering on the way to the P1 counter limited the proton angle to a maximum of about 55^0 at the lowest energy (141 MeV), corresponding to a minimum pion angle of $\approx 55^0$. For most runs ("set A"), the forward–most pion arm was set at 60^0, corresponding to a P1 counter angle of 53^0 at 141 MeV. The backward–most pion angle was limited to 155^0 by the requirement that the corresponding proton counter angle at 267 MeV (8.6^0) be situated safely outside the cone of the incident beam.

2. Forward Angle Single–Arm Pion Detection

For pion angles less than about 50^0, the corresponding proton energies were not large enough for the protons to escape from the liquid hydrogen target (described in the following section). Consequently, a set of π^+ runs at forward pion angles were undertaken at $\theta_\pi \in \{20, 30, 40, 50, 60, 70\}$ degrees with the proton arms removed from the EVENT coincidence. In this case an ARM$_i$ event was defined by the coincidence BEAM$\cdot\Pi_i$

Candidate πp events were identified by the TOF to the π2 counter. In these single-arm liquid hydrogen target runs, the foreground-to-background ratios were considerably poorer than in coincidence mode, ranging from about 1.5:1 at 20^0, to about 7:1 at 70^0. A sample spectrum is illustrated in Fig. 5. The reactions which contributed the bulk of the π^+p single-arm background included: pion elastic scattering from the mylar windows and domes in the target (carbon, oxygen, and hydrogen), pion quasi–elastic scattering from these materials (mainly carbon), and π^+ absorption on quasi–deuterons in these same nuclei, producing two fast protons which could satisfy the Π timing gate. However, despite the sizable backgrounds, reliable background subtraction was possible. The single-arm runs were set up with the target oriented at -39.4° so that the downstream window faced the middle pion arm. The pion angles were chosen to fill in the angles not already covered by the two-arm coincidence runs, with some overlap to provide a consistency check. The forward-most angle was limited by the requirement that muons arising from decay of beam pions would not cause a pion arm coincidence.

C. Targets

Since the use of solid targets in πp elastic scattering experiments has been the subject of some criticism [35], the coincidence measurements were taken with both thin solid CH_2 and a novel flat-walled, super-cooled liquid hydrogen (LH_2) target in order to lay this concern to rest. Although most of the measurements described in this paper were done using the LH_2 target, several measurements were repeated using the solid targets as a check on systematic uncertainties.

The solid CH_2 targets consisted of 127 x 127 mm^2 square slabs of ρ=0.93 gm/cm^3 CH_2, with a slab of 100 x 100 mm^2 square carbon graphite used for background measurements. The targets used and their respective thicknesses are shown in Table I. The densities were obtained from measurements of the linear dimensions together with weights measured using a Mettler balance. The uniformity of the linear thicknesses was checked using a machinist's comparator, specified to be accurate to 2.5x10^{-5} mm [48]. The hydrogen and carbon contents of the CH_2 targets were determined to 1% accuracy by chemical analyses provided by a commercial laboratory [48]. The stopping power for pions and protons in the graphite background target was midway between those of the CH_2 'D' and 'E' targets, the solid targets which were most often used in the experiment. Incidentally, these were the same targets used in the experiments of Brack et al. [28,49].

The targets were supported by thin aluminum frames attached to an aluminum support bracket, and the whole assembly was mounted onto a machinist's rotating table to provide accurate and reproducible angular adjustment. A transit mounted downstream of the target position was used to check the 90^0 orientation ('edge on') of the target after every change or adjustment of the target angle. The 0^0 orientation was set by attaching a mirror to the target, and then shining a He-Ne laser through the transit viewpiece with the reflected light required to project back onto

the laser exit aperture. In this way, the target angles were determined to $\pm 0.25^0$ (68% confidence). The CH_2 target angle was fixed at 53.0° at all energies except 218.1 MeV, where it was 50.0°.

A key element in the experiment was the development of the thin, flat–walled, super-cooled liquid hydrogen target. This target was thick enough to provide protons at high density within a cell of accurately known thickness, yet thin enough that energy and interaction losses to the incoming and scattered beams were minimal, as were the corrections to the effective solid angles due to extended source size effects. Some construction details of the target, including relevant physical parameters, are displayed in Fig. 6. The LH_2 target was contained within the 14.99±0.03 mm thick hollow stainless steel ring and two prestressed mylar windows. The liquid hydrogen in the target was cooled by a separate source of liquid hydrogen flowing inside the hollow stainless steel ring. This cooling hydrogen was liquefied once at the beginning of the experiment and then maintained at 15.6 to 16.0 psia. The liquid hydrogen in the target itself, however, was maintained at 18.05±0.05 psia, i.e., approx. 2.2 psia overpressure (i.e. "super-cooled") in order to prevent boiling and bubbling in the target. The entire target assembly was contained within a large cylindrical stainless steel vacuum vessel. An inner copper heat shield at the target hydrogen temperature and an outer shield at liquid nitrogen temperature, both surrounded by aluminized–mylar superinsulation, prevented transmission of infrared radiation onto the target and thus further ensured that no bubbles formed. Two gaps in the vacuum vessel covered by kapton windows provided beam access and egress.

Prestressed mylar windows on the target cell were used to keep the linear thickness of the target as uniform as possible. The deflection due to differential pressures across the window was measured on a test bench at liquid nitrogen temperatures as 1.83 mm/psid [50]. Although quite small, this would still cause unacceptable bulging if the target cell were contained in vacuum. Consequently, the cell was capped on both sides by 0.229 mm thick mylar domes containing gaseous helium at a pressure regulated to within 10 mpsid of the pressure in the cell, causing a maximum ±0.0356 mm fluctuation in the cell width. A 140±10 mm liquid hydrogen column above the target centre to the pressure regulation point produced a 14±1 mpsid hydrostatic head resulting in a net 0.026±0.002 mm outward window deflection at the bottom of the target. The helium pressure and target–helium pressure differential were digitized and read–out online at regular intervals by the data acquisition system. The linear thickness of the LH_2 target between the inside surfaces of the mylar windows was 15.04±0.06 mm, comprised of 14.99 mm from the machined depth of the ring, a correction taking into account shrinkage when cooled to 20K, bulging of the windows due to the hydrostatic head, and also a thin layer of epoxy bonding the windows to the ring. The total uncertainty is the sum in quadrature of the individual uncertainties.

Target empty data for background measurements were obtained by evacuating the target cell of all the LH_2 and residual gas, and replenishing it with helium from the domes. The helium pressure was adjusted to maintain the same areal thickness as in target full operation: 15.8 psia at a target angle of 53.6^0 and 16.1 psia at -39.4^0.

Due to a failure of the target vapour bulb transducer at the beginning of the experiment, the target cell temperature could not be monitored continuously, but was determined instead at four occasions spanning the entire experiment by using the target cell itself as a vapour bulb. The vapour pressure at the LH_2 boiling point when the target was half full was provided by the helium pressure transducer together with the differential pressure transducer, both of which were regulating throughout this process. The resulting temperatures, inferred from vapour pressure tables [51], were 20.63, 20.58, 20.56, and 20.55±0.02K, respectively, where the last value includes a small correction which reflects the roughly 8% ortho-(normal-) to para–hydrogen conversion which occurred during the 16 hours after the target was filled. The observed temperature drop is consistent with normal- to para–hydrogen conversion in the cooling condenser fluid, which was kept at a constant average pressure throughout the run. The target densities at each temperature were inferred from molar volume vs. temperature tables [51]. The average of the normal- and para–hydrogen densities was used since the exact value of the normal/para ratio was unknown. Although for most runs the conversion from normal to para (about 0.5%/hour for the first 100 hours) would not have proceeded very far under normal conditions, unknown catalytic effects might have sped up the process. This introduces a 0.2% uncertainty to the target density, a value which completely dominates that arising from the temperature uncertainty of 0.02% (0.01K). Combining the measured linear thickness together with the known average target density throughout the run, the target areal density was determined to be 106.2±0.5 mg/cm^2, or 63.43±0.32 10^{-6} mb^{-1}.

The 0° angular orientation of the target was set during the experiment by using a transit to view markers which were placed onto the lower rim of the vacuum vessel during target assembly. An overall target angle uncertainty of $\pm 0.3^0$ was estimated based on these mechanical measurements. The target angle was set by rotating the entire cryostat, with the angles read off a large disk on the support structure to an estimated reproducibility uncertainty of 0.2°. The LH_2 target angle was fixed at 53.6° for the "Set A" pion angle settings, and 50.6° for the "Set B" settings.

1. Tests of the LH_2 Target Angle/Thickness

To check whether there was a systematic offset in our nominal angles, two–arm π^+p coincidence data were taken at 168.8 MeV with nominal LH_2 target angles of 45^0, 53^0 ("normal"), and 60^0. The "Set B" π^+ data (at 50°) at this energy were also considered by interpolating the data to the "Set A" angles. Small uncertainties from the interpolation were added to the interpolated data. The effect of a 0.2° target angle reproducibility uncertainty was added to all points. The results are shown in Fig. 7, which include one point at $\theta_\pi^{\rm lab}$=60° from the forward angle single–arm data using a nominally -40° target angle. The results for each of the six pion angles were then fitted to a form $\cos(\theta_{\rm tgt}+\theta_0)/\cos(\theta_{\rm tgt})$. The fit yielded a common offset of 0.86±0.36°. Neglecting the outlier point at $\theta_\pi^{\rm lab}=115°$ for $\theta_{\rm tgt}=60°$, the offset became 0.6±0.4°.

Midway through the experiment, an independent measurement of the target thickness was performed, involving the use of silicon counters [52] to measure the energy loss of beam protons passing through the LH_2 target. The technique is described in detail in Ref. [33]. The target was rotated to four nominal settings: -40.0, 0.0, 38.5, and 53.0^0, this last angle being the setting for most of the two-arm production runs. Fitting the data to the expression $X = X_0/\cos(\theta+\theta_0)$ yielded : X_0= 104.4±0.8 (stat.)±1.7 (norm.) mg/cm^2, θ_0= 0.7^0±0.4^0. Although the results from the latter three settings were perfectly consistent with that of the vapour bulb technique (Fig. 8), the -40.0° point was substantially lower, implying a systematic overall 0.7±0.4° angular offset[5]. Additional evidence for a systematic angle offset was provided by the single–arm results, which overlap better with the two–arm results at their respective energies if an offset of about 0.5-0.7° is assumed. Final compromise values of θ_0=0.6±0.4° with X_0 = 106.2±0.5 mg/cm^2 (from the vapour bulb result) were adopted and applied to all the data taken with the LH2 target. This value is consistent with all the available evidence, while discounting to some extent the effect of the outlier points at $\theta_\pi^{\rm lab}=115°$ for $\theta_{\rm tgt}=60°$ in Fig. 7, and the -40° point in the target thickness measurement. The resulting uncertainty in the LH_2 target angle is the dominant source of normalization uncertainty in all data taken with that target (as indicated in Table II).

2. Foreground and Background Running

Several hours were required to fill or empty the liquid hydrogen target, so it was not possible to conduct a target empty run immediately after completion of each target full run, or vice versa. Therefore, a series of target full runs was carried out for each configuration of the TOF spectrometer and target, followed by all the respective target empty runs. During target emptying (filling), the target would be moved out of the beam, and the time used to conduct measurements with the solid targets.

For the case of the CH_2 targets, data runs were followed immediately by the graphite background runs, except during those π^+ runs at 169 MeV designed to explore systematic effects. As only the two–arm coincidence configuration was employed for the solid targets, the effect of a relative foreground/background normalization uncertainty on the cross sections was negligible (<0.1%) due to the very low level of background characterizing this arrangement.

D. Data Acquisition

The pulse height and timing signals from every scintillator in the system were recorded using CAMAC electronics and read–out by computer to 8 mm video tape using the TRIUMF VDACS [53] data acquisition program. Both the individual and the meantime signals from the proton counters were time digitized and scaled. As well, all the various counter coincidences were counted by scalers. In particular, the BEAM output was fed into two independent scalers as a consistency check. The scalers accumulated continuously when the data acquisition was active, and were read–out by the CAMAC system at approximately one minute intervals during a run as well as the end of a run.

The EVENT gate consisted of the logical OR of all six pion–proton pair coincidences (or just pion arms for single-arm runs) together with the beam sample signal (SAMPLE) : EVENT $\equiv \sum_{i=1,6}{\rm ARM}_i + {\rm SAMPLE}$. The LAM signal, which formed the ADC gates, TDC starts, and triggered the event readout, was the EVENT signal gated by additional "inhibits" depending on whether or not the computer was busy ($\overline{\rm BUSY}$), whether the beam was turned off (detected using a rate meter), or whether another EVENT signal had immediately preceded the current one (detected using a

[5]The data could also be explained in terms of a $+1.5^0$ shift at the -40° setting, since during the thickness measurement, the target was positioned to that angle with some difficulty.

fast inhibit). The live time (or duty factor) (f_{LT}) of the data acquisition system was determined from the ratio of LAMs/EVENTs.

The ADC gate widths were set at approximately 30 ns, wide enough to include essentially all the signal, but smaller than the beam repetition period of 43 ns to avoid the possibility of pile–up and random coincidences. The TDCs operated in common start mode, with the LAM as the common START.

In order to reduce the number of ADC and TDC channels required to accumulate all the data from the six pion and proton arms, a multiplexing scheme was employed, whereby the only ADC and TDC words (from π1, π2, and P1) recorded by CAMAC were those for the arm which detected the πp EVENT. To determine which arm caused the EVENT, the ARM_i timing signals for *each* of the six arms, as well as the beam SAMPLE signal, were fed to separate channels of an input register and processed by the CAMAC J11 Starburst controller. This system also indicated whether more than one arm recorded a hit for the same EVENT, thus giving another measure of the rate of accidental coincidences. In practice, the largest number of multiple events observed for any run was two out of many thousand events.

III. DATA ANALYSIS

The centre-of-mass differential cross section at laboratory kinetic energy T_π at centre–of–momentum scattering angle θ_{cm} was determined using:

$$\frac{d\sigma}{d\Omega}(T_\pi, \theta_{cm}) = \frac{Y(T_\pi, \theta_{lab}) \cdot \cos\theta_{tgt} \cdot J(T_\pi, \theta_{lab})}{N_\pi \cdot \Delta\Omega_{eff}(T_\pi, \theta_{lab}) \cdot N_{prot} \cdot \epsilon} \tag{2}$$

where Y = number of detected πp events at laboratory angle θ_{lab}, θ_{tgt} = target angle, N_π= number of beam pions incident on target, $\Delta\Omega_{eff}$ = effective laboratory solid angle for πp detection, N_{prot} = number of target protons/cm^2, ϵ = scintillator efficiencies, and J is the Jacobian transformation from the laboratory to centre-of-mass reference frame. The target proton densities are listed in Table I. Each of the other terms in Eq. 2 are discussed separately in the following sections. Details of the Monte Carlo determination of $\Delta\Omega_{eff}$ are presented in Appendix A, while the techniques employed for analysis of the scintillator signals are presented in this section. The final cross section results are presented in Sec. IV.

A. Solid Angle

The effective solid angle of a pion arm (for single–arm operation), or pion and proton arm combination (for two–arm coincidence mode) was determined by Monte Carlo simulations. As the time-of-flight difference spectra were unable to distinguish between scattered pions and those muons arising from the decay of scattered pions, the net πp yield consisted of those events in the pion arm involving a pion *or* a muon, and a proton in the proton arm in the case of two–arm runs, all of which needed to be modelled as faithfully as possible. The consistency of the simulation results with the many experimental checks that were carried out was an important check of the procedure used and provided a useful measure of the magnitude of many of the systematic errors characterizing the experiment.

In both the two-arm and single-arm operational modes, the solid angle subtended by the π2 counter (2.646$\pm$0.013 msr) defined the geometric solid angle ($\Delta\Omega_{geom}$) for detecting scattered pions. However, some of the scattered pions (protons) that should have struck a π2 (P1) counter failed to do so, whereas some outside the geometric solid angle were actually detected. Consequently, an effective solid angle $\Delta\Omega_{eff}$ was introduced to compensate for these competing effects. Various factors contributed to the effective solid angle. A pion (proton) could suffer *interaction loss* by hadronic elastic or inelastic scattering on the way to the π2 (P1) counter, and thus escape detection. The resultant decrease in the effective solid angle was substantial, ranging from about 2% to 5% depending on target and pion scattering angles. The non-zero pion beam size resulted in an *extended source* in the target from which a scattered pion could originate, making the distance to the π2 counter (hence the solid angle) different for each pion. Although the effect was small, <0.2%, nonetheless the determination of $\Delta\Omega_{eff}$ involved the weighted average over the extended source. A scattered particle that would otherwise have missed the π2 (P1) counter could suffer (Coulombic and hadronic) *rescattering from an experimental structure* and subsequently hit a counter. This effect was significant only when using the LH_2 target in the single pion arm setups or for the most forward pion arm in the two-arm setup. In the former case, pions could rescatter hadronically from the stainless steel target vessel and subsequently cause a pion arm coincidence. In the latter case, pions that would have missed the pion arm counter could have scattered off the target ring and subsequently hit the counter. In the worst cases, rescattering caused up to $\sim$2% effect in the effective solid angle. *Pion decay* was another source of pion loss, amounting to a net reduction of $\Delta\Omega_{eff}$ by 2–4%

(see Fig. 9). The presence of the intermediate $\pi 1$ counters constrained the number of daughter muons detected from pions that would not have been detected otherwise. In the absence of multiple scattering, the TOF spectrometer was designed so that for a monochromatic, point scattering source, every proton conjugate to a pion that hit the $\pi 2$ counter would hit the corresponding P1 counter. However, the combination of an extended source, beam momentum spread, multiple scattering, and pion decay, spread out the recoil proton distribution. The net result of the *proton counter constraint* was a (typically) 7% reduction in the effective solid angle as illustrated in Fig. 9. Finally, particles entering near the edge of the scintillator could exit out the side, thus reducing the path length and consequently the light output in the scintillator. However, as most events of this kind would have still yielded a detectable signal due to the low thresholds used in this experiment, such corrections were expected to be <0.1%.

1. GEANT Monte Carlo Determination of Solid Angles

Due to the correlations among the various effects described above, the only way $\Delta\Omega_{\rm eff}$ could be determined accurately was by a *full* Monte Carlo simulation of the πp scattering process in the TOF spectrometer. All the relevant physical processes associated with πp scattering (multiple scattering, pion decay, etc.) together with the details of the experimental configuration (scintillators, target, air, etc.) were included. By generating a number $\rm N_{mc}$ of πp scattering events, where the scattered pion was randomly and uniformly distributed within a solid angle $\Delta\Omega_{\rm mc}$ chosen to be large enough to accommodate all events which could possibly result in a $\pi 2$ hit, the *effective* solid angle $\Delta\Omega_{\rm eff}$ was given by : $\Delta\Omega_{\rm eff} = \frac{\rm N_H}{\rm N_{mc}} \cdot \Delta\Omega_{\rm mc} \quad \left(\pm\frac{100}{\sqrt{\rm N_H}}\%\right)$ where $\rm N_H$ was the number of $\pi 2$ counter hits in the simulation. The uncertainty is that expected from the Poisson limit to the applicable binomial statistics.

The GEANT [54] detector description and Monte Carlo particle tracking program was used to simulate the πp scattering reaction in the TOF spectrometer for every target, target angle, pion angle, trigger configuration. All elements of the TOF spectrometer were accurately modelled, including composition, dimensions, and positions of all in–beam, pion arm, and proton arm counters as well as relevant characteristics of the CH_2 targets (when employed). The LH_2 target was also faithfully modelled, including all windows, dome, heat shield and super–insulation layers, stainless steel vacuum vessel, target cooling ring, and liquid hydrogen coolant in the ring (see Fig. 6 and others in [33]). Accurate modeling of this kind ensured proper treatment of the effects due to interfering structures that were discussed previously. All the relevant physical processes were included in the simulation, though in most cases the hadronic interaction routine was not, since it was found to be too imprecise for calculating nuclear absorption losses in the low energy region relevant for this experiment. These small interaction losses were subsequently introduced by hand to obtain the final results. Details of the simulation are described in Ref. [33], while some details concerning the hadronic interaction corrections introduced subsequent to the discussion found in Ref. [33] are presented in Appendix A.

2. Tests of the Effective Solid Angle Determination

The solid angle results from the GEANT simulations showed that effects of the $\pi 1$ and/or P1 counters affected the geometric solid angle subtended by the $\pi 2$ counter by no more than ≈9% in the *worst* case, and more typically by only ≈5%, while the other effects (multiple scattering, etc.) were even smaller. Thus *a priori* it would be expected that the systematic uncertainty introduced by these various effects should be smaller than about 1% (i.e., 10% uncertainty of the corrections).

Nevertheless, to test the reliability of the effective solid angle determinations, π^+p data sets at 168.8 MeV were obtained under various experimental setups which differed from the standard two–arm configuration. For example these included deliberately misaligning the proton P1 counters by $+0.25^0$, changing the P1-target distance from 920 mm to 855 mm or 1020 mm, removing the $\pi 1$ counter from the EVENT coincidence, removing the P1 counter from the EVENT coincidence (i.e. single–arm mode), and increasing the incident beam momentum spread to 3% Δp/p (from 1%). The resulting cross-sections are shown in Fig. 10. Although the effective solid angles varied by as much as 5% among the various configurations, it is evident that all the data are consistent at about the 1% level.

In addition, two–arm π^+p coincidence runs at 168.8 MeV utilizing different solid CH_2 targets were obtained to provide information concerning the relevant sizes of the uncertainties associated with the target proton density (1%), the effect of hadronic interaction losses in the target on the incident beam normalization, and the effect of varying scattered particle multiple scattering and hadronic interaction losses on the solid angle determination. Data were accumulated for CH_2 target thicknesses of ≈0.5 mm (target "A"), 2.0 mm ("D"), 3.2 mm ("E"), and 5.2 mm ("D"+ "E"). The relative cross section differences for each of the targets are shown in Fig. 11. The error bars shown are purely statistical. The beam pion losses varied from 1.2% for target A to 2.4% for target E+D, while the modification of the effective solid angles associated with these targets varied between 6.5% and 1.5% at the extremal angles, due

to different proton energy losses and hadronic interaction losses. The results are completely consistent within the relative normalization uncertainties. The solid and dashed horizontal lines in Fig. 11 are the weighted averages of the cross section using the three thinnest targets and are included to better visualize the results. Considering the order of magnitude change in target thickness between target A and E+D, these results provide confidence that the solid angles and other target-dependent uncertainties are well understood.

B. Beam Intensity Determination

The number of incident pions N_π per run involved a product of six terms:

$$N_\pi = B \cdot f_{LT} \cdot f_\pi \cdot f_D \cdot f_L \cdot f_S \tag{3}$$

where B = BEAM coincidences recorded by hardware scalers, f_{LT} = data acquisition live time fraction (efficiency), f_π = pion fraction to the channel exit, f_D = pion survival fraction (decay) from channel exit to target centre, f_L = pion survival fraction after interaction losses to target centre, and f_S = correction factor accounting for multiple pions traversing the target. Each of these factors is discussed in detail in the following sections.

1. Beam, B and livetime, f_{LT}

The number of BEAM coincidences, B, was counted in two separate CAMAC scaler modules. As mentioned in Sec. II D, the live time f_{LT} was measured as the ratio of the CAMAC scalers LAMs/EVENTs. These values were checked using visual scalers. Since all three scalers recorded large values with no discrepancies, B and f_{LT} were considered to be virtually error–free.

2. Pion Fraction, f_π

Determination of the pion fraction f_π proceeded in two steps: removal of the proton contribution in the beam, and determination of the beam contamination due to muons and electrons originating near the pion production target. Protons were effectively removed from the BEAM by means of differential energy loss within the channel provided by a midplane absorber before the second bending magnet, and a $\overline{\text{S2BH}}$ upper level discriminator used to reject the residual (large pulse height) protons. However, at the highest two beam energies involved in the experiment, some protons managed to leak into the BEAM definition. These protons were easily identified by the TCAP SAMPLE spectrum and large pulse heights in all the in–beam counters. As the corrections due to these protons were never large (<0.5%), their presence only introduced a small additional uncertainty to f_π (<0.1%).

The muon and electron contamination of the pion beam arising from pion decay near the pion production target was readily determined using particle TOF to the S2B counter. At low beam energies ($\leq$ 110 MeV), the length of the channel allowed all three components to be easily resolved during normal operation [28]. However at higher energies, the poor time resolution imposed by the normal 3 ns width of the proton beam buckets limited the clean separation of particles, and, for most of the energies involved in the experiment, this limitation meant that the muon (and at the highest energies even the electron) components were obscured by the dominant pion peak. Consequently, a series of runs with a reduced proton pulse width were dedicated to measuring the beam composition. As illustrated in Fig. 12, the ≈1 ns wide Gaussian distribution achieved in this "phase–restricted" mode of operation was significantly narrower than the ≈3 ns double–Gaussian time structure seen during normal runs.

Two sets of phase-restricted runs were carried out at all the energies involved in this experiment, using the same pion production target and midplane absorbers employed in the data production runs. The midplane slits were set to 0.5% $\frac{\Delta p}{p}$ in the first series of measurements, and 2% in the second, with the jaws set at a value midway between those used in the normal π^+ and π^- runs. In addition, some runs were obtained with the momentum slit widths varied between 0.5% and 2.5%. Since only beam counter information was required for these tests, all pion and proton arms were removed from the EVENT definition. The π:μ:e ratios were determined from Gaussian fits to the TCAP timing spectra. All three peaks were cleanly separated except at the highest two energies, where the muon peak was obscured by the tail of the pion distribution. However, by fixing the muon peak position using the expected π–μ and μ–e TOF differences at those momenta, robust fits were found. The electron component could be clearly separated at all energies.

The pion fraction results (f_π) from the two series are summarized in Fig. 13. Immediately obvious is the difference in the π^- results between the two series, ranging from 2% at 140 MeV to 0.5% at the highest energy. On the other

hand, the π^+ results from the two series differed by less than 0.2% at all energies. Such results are not unexpected. As the muons originate from a more distributed source at the production target, and so are not focussed as well as the pions at the midplane, the $\pi/(\pi+\mu)$ fraction should depend on midplane slit setting. Consequently, narrow slit settings favour the pions over the muons. This effect was expected to be even larger for the electrons, since their source was even more spatially distributed, and they were a much larger fraction of the π^- beam than were the muons. The experimental results confirmed this. As there were many fewer muons and positrons in the π^+ beam, such effects were much less significant there. The REVMOC [55] simulations also showed that the fractions depended on the geometry of the beam counters, since larger (smaller) counters would intercept a larger (smaller) fraction of the muons and electrons which tend to form a halo around the pion beam. Because of this dependence, our results cannot be compared directly to those of Ref. [56] where the phase–restricted beam technique was also used. However, the trends observed here are consistent with those shown in that work. Tests with the position of the proton beam deliberately varied on the production target showed that the above results were insensitive to the typical amount of beam variation monitored by our beam hodoscope during our runs.

The results shown in Fig. 13 demonstrate that the π^+ fraction was $\geq$98% at all energies, and the results of the two series were consistent to $\approx \pm 0.1\%$. These results were used for f_{π^+} at all energies. However, in the case of π^-p, multiple Gaussian fits were performed on the TCAP spectra during normal operation in order to fine-tune the results of the run in question. Although the muon contribution in the TCAP spectra was obscured by the pion peak during normal running, the electron peaks could be easily identified for incident pion energies up to 218 MeV. Because the time structure during normal operation resulted in 2 (sometimes 3) well-defined timing peaks, multiple Gaussian line shapes were fit to the pion peaks, with the phase-restricted beam results used to constrain the muon and electron peak amplitudes and centroids. A typical fit overlayed on the TCAP beam SAMPLE spectrum is illustrated in Fig. 14. During normal beam operation, the timing spectra possessed small "right hand" tails. The fact that these tails were due to pions and beam contamination was inferred from the fact that they were apparent for single πp events, of the form $\Pi\cdot P\cdot\overline{\text{VETO}}$ EVENT, since only pions could yield a (pion arm)–(proton arm) coincidence. By fitting the electron peak together with the pion tail, the electron fraction could be readily determined. As the phase–restricted beam results indicated that the $\pi/(\pi+\mu)$ ratio varied by less than 0.2%, f_π could be reliably estimated. In all cases, the π^- results were within the range of values of the two phase-restricted beam series, whereas the π^+ results were within 0.2% of the phase-restricted beam values. At the lower energies where the electron component could be reliably estimated, the results for f_π extracted in the above manner were used in the cross section calculations, whereas at the higher energies, the phase-restricted beam results were used. Since the π^- results were always between the results for the two phase-restricted beam series, the estimates at the higher energies were not expected to vary by more than $\approx$0.5% from those shown in Fig. 13.

The precise nature of the quantity, f_π, should be emphasized here. Since muons from those pions which decay *after* the channel exit could not be distinguished from pions by TOF (see Fig. 16), the "pion fraction" defined above contains a contribution from these decay muons. The fraction f_π thus represents the fraction of the beam at the last channel element that consists of those pions, muons, and electrons that would *subsequently* cause a BEAM coincidence. However, to obtain the fraction of BEAM coincidences due to *pions* in the *target*, f_π had to be corrected for pion decay in the channel and downstream of the channel exit (f_D) and for hadronic interaction losses (f_L).

3. Pion Decay, f_D

Pion decay downstream of the last channel element, f_D, was calculated in a straightforward fashion by Monte Carlo simulation using the GEANT [54] program. Neglecting hadronic interaction losses, the factor f_D represented the fraction of the pions at the exit (quadrupole) magnet midplane which would subsequently produce a BEAM coincidence and hit the target. Since this factor was dependent on the beam counter geometry and beam phase space, the simulations were carried out for each run using the beam phase-space parameters measured during the channel tuning phase of the experiment. The results for f_D varied between 0.961 at 141 MeV and 0.973 at 267 MeV, and were rather insensitive to the beam size. Considering the decay correction only up to the S2B counter, the pion survival fraction was 0.992, virtually independent of energy and beam size. As the energy increases, fewer pions decay, but since the muon cone angle is smaller, more of the decay muons are detected. These GEANT results for the pion decay to the S2B counter and to the target were checked using the REVMOC [55] beam transport program, with the two simulations agreeing to better than 0.1% at all energies.

One source of muons not yet discussed was that originating from pion decay within the channel. As the muons appearing in the muon peak possessed the largest TOF difference with respect to the pions, they originated near the production target. Since the $\pi-\mu$ TOF difference for muons originating after the last channel magnet was smaller than the instrumental timing resolution, they would consequently appear under the pion peak. Muons originating between

the production target and the last magnet would have a timing distribution spread between these two extremes. The results from the lower energy phase-restricted beam fits show that the size of this contribution was significantly smaller than that from the muons originating from the production target, since a clear gap existed between the pion and muon peaks. The contribution was expected to be small since most decay muons emerge at an angle to the direction of the incident pion (the "Jacobi angle", varying from $\approx 9^0$ at 140 MeV to $\approx 6^0$ at 270) with a momentum different from the pion, so these muons would either strike the beam pipe walls or be bent away from the rest of the beam by the magnets. Nevertheless, a Monte Carlo simulation of the pions and their decay muons from the production target through the beam line to the in–beam counters and scattering target was undertaken using the REVMOC [55] beam transport program [33]. Fig. 15 shows the pion beam phase space parameters for two settings of the rate restricting jaws, demonstrating that the channel was well understood. This simulation confirmed that the contamination from muons originating between the production target and the channel exit was small, amounting to only about 0.2±0.1%. This is seen clearly in Fig. 16, which shows the time distribution of pions and muons originating from various points in the channel. Therefore the correction $f_\pi \rightarrow 0.998 \cdot f_\pi$ was utilized in the beam normalization factor for all data–taking runs.

4. Pion Beam Interaction Losses, f_L

Although the simulations discussed above neglected pion loss through hadronic interaction since neither the REVMOC nor GEANT simulations of these interactions were sufficiently reliable for this application, the factor f_π *already included* hadronic loss effects to the S2B counter, since it was measured experimentally in the phase-restricted beam runs. Therefore, the only hadronic losses of pions that remained to be accounted for in the beam normalization factor were those in the CH_2 or LH_2 targets (and shields, windows, etc. in the case of the LH_2 target), in the air, and in the S2B counter (*after* a hit had been registered by the electronics). All the pions which interacted in the air and in the various shields and windows surrounding the LH_2 target were assumed lost, since it was very unlikely that such pions would continue forward to the target. For the S2B counter, pion losses in the tape on the downstream face of the counter and in the final third of the scintillator were included. The maximum total hadronic loss correction calculated in this way was ≈2.0% for the case of 168.8 MeV π^+ in the LH_2 target oriented at 60^0, with the largest contribution being that of pion loss to inelastic channels in the target. The uncertainty in this value due to the various assumptions and hadronic cross section estimates was estimated to be about 10% arising from the uncertainties in the pion–nucleus cross section estimates with an additional 10% due to the assumptions concerning the interaction losses, implying a loss correction for the above case of ∼2±0.3%.

5. Multiple Pion Correction, f_S

For a ∼1 MHz pion rate, implying delivery of a pion to the target area in only one out of every 25 beam buckets, the problem of signal pile-up characteristic of high intensity, low duty factor accelerators was negligible, since at these rates, using Poisson statistics, the probability of multiple pions in a single beam bucket was only about 3%.

A BEAM coincidence would indicate only that *at least one* particle had passed through all the beam counters, regardless of how many pions were delivered in a single beam bucket. Therefore, when calculating cross sections, either the total beam counts, B, had to be increased appropriately to correct for events with more than one incident pion, or these events had to be rejected outright from the analysis. As a consistency check, both approaches were employed when determining the single–pion beam correction factor, f_S.

The first of these methods, involving correcting the beam counts, B, was called the "Poisson" correction scheme since the number of pions occurring in a single beam bucket was described by Poisson statistics. In beam counter geometries where all the pions which could have reached the target must have passed through the counters, the correction to B would have been straightforward: if the probability of a pion occurring within a beam bucket is λ_B (typically several percent), and ν is the frequency of the beam buckets (23.058 MHz), then the actual rate of pions traversing the beam-defining counters would be $\lambda_B \cdot \nu$, whereas the rate indicated by the counter scalers would be the rate of one or more pions per bucket, or $\nu \cdot (1 - e^{-\lambda_B})$. Therefore, the correction factor for the beam-defining counters would have been $f_S^p = \lambda_B/(1 - e^{-\lambda_B})$

In our case, however, a small portion of the pion beam *missed* the beam-defining counters, yet still traversed the target. Consequently, if one or more pions traversed the target *in addition* to the one which travelled through the beam counters, the chance of a πp interaction would have increased correspondingly. If the probability per beam bucket of finding a pion able to traverse the target was λ_T, (thus a true pion rate on target of $\lambda_T \cdot \nu$), then the probability that the pion *also* passed through the beam-defining counters was $\rho = \lambda_B/\lambda_T$ and the probability that

it missed was $\gamma = 1 - \rho$. In this case, the actual pion rate traversing the target *and* associated with a count in the beam counters is $R^{\pi}_{\rm beam}$=$\nu\lambda_T(1 - \gamma e^{-\lambda_B})$, which replaces the $\lambda_B \cdot \nu$ used previously. Thus the multiple pion beam correction f^p_S for the case where the beam counters do not intercept all the incident beam is:

$$f^p_S = \frac{\lambda_T(1 - \gamma e^{-\lambda_B})}{1 - e^{-\lambda_B}} \tag{4}$$

To use Eq. 4, λ_B was obtained in a straightforward fashion from the observed rate of pions hitting *both* the BEAM counters *and* the target ($R^{\pi}_{\rm beam}$). Determination of the rate of pions traversing the target ($\nu \cdot \lambda_T$) had to be inferred from the observed VETO counter rate ($\nu \cdot (1 - e^{-\lambda_V})$), with γ given as above. The VETO counter was designed to intercept the entire pion beam in the idealized case of no decay and interaction losses. These losses were accounted for using our REVMOC [55] beam simulation to obtain the correct target pion rate and fraction from the observed VETO rate. These simulations showed that for π^+ beams, where the electron contamination was very low, the pion rate at the target was 97±0.3% of the VETO rate for all energies involved in the experiment. The simulation results were confirmed by test runs using a 15 cm diameter scintillator target (the same size as the LH_2 target) with two different beam intensities, 1 and 2 MHz. For π^- beams, the pion rate on target varied from about 85% of the VETO rate at 140 MeV to about 95% at 267 MeV. The multiple pion correction factor, f^p_S, was quite insensitive to the approximations involved in the REVMOC modelling for the beam intensities involved (≈1 MHz through the in–beam counters and ≈1.5-2 MHz on target). At these intensities, a ±5% variation in the target rate corresponded to $\delta f^p_S \approx \pm 0.4\%$.

The second of the multiple pion correction methods, outright rejection of such events, also was realized using the VETO counter. Since the chance of two pions in a single beam burst *both* interacting in the target was exceedingly small, then if one pion interacted causing a πp event, the other would pass through the target and be detected by the VETO counter. Such events were readily eliminated from the πp yields and the accumulated BEAM hits, B, were corrected appropriately. Using similar notation to that of the previous section, the appropriate multiple pion "veto" correction factor was f^v_S = (BEAM events hitting target with only 1 pion in bucket)/(measured BEAM). That is:

$$f^v_S = \frac{(\lambda_T e^{-\lambda_T}) \cdot \rho}{1 - e^{-\lambda_B}} \tag{5}$$

Since λ_B was known, and λ_T and ρ obtained as described above, Eq. 5 was easily evaluated.

6. Test of Multiple Pion Corrections

To test our two prescriptions for the multiple pion correction factor, two-arm π^+p data at 168.8 MeV were obtained for five pion beam rates on the LH_2 target: 0.34, 0.87, 1.4, 3.1, and 6.7 MHz. One empty target run with a 1.5 MHz rate was used for background subtraction in all cases. Since the beam rate was adjusted using the front end jaws of the pion channel, the pion beam size on target also changed. However, GEANT simulations showed that the effect of the jaw changes on the experimental solid angle was less than 0.2%. Consequently, the solid angles corresponding to the normal beam size were used in all cases. The cross section results are displayed in Fig. 17. The beam correction factors varied from 1% at 0.34 MHz, 4% at 1.4 MHz, to 26% at 6.7 MHz. The maximum difference between the cross sections corrected by the VETO and Poisson schemes was 0.3% at 6.7 MHz, and smaller at the lower rates. As is evident from this figure, no monotonic systematic variation within the statistical uncertainties (≈1.3%) was observed in the cross sections over this range. For all two–arm production $\pi^{\pm}$p runs, the cross sections corrected by the Poisson and VETO schemes never differed by more than 0.3%, the former being usually slightly larger than the latter, consistent with expectation based on those events which should have been vetoed but were not, as discussed in Sec. III C 1. The average of the Poisson and VETO corrected cross sections were used for the two–arm results.

However, for the single–arm π^+p runs at 141.2, 168.8, and 218.1 MeV, a much larger variation in the cross sections calculated with the two correction schemes was observed. The Poisson correction factors for these runs were the same as those for the two-arm runs (at the same beam rate and energy), whereas the VETO correction factors were considerably larger, especially for the target empty runs. Although the average discrepancy between the Poisson and VETO corrected cross sections averaged only about 0.7%, a systematic dependence with angle was observed, with the VETO–corrected cross sections 1-2% smaller than the Poisson corrected results at 20°, increasing to be similarly larger than the Poisson at 70°. Since the Poisson scheme relied solely on the measured beam rates, the resulting correction should have been independent of pion angle as indeed was observed. The most likely explanation is that pion reactions on the background nuclei (mostly carbon) resulted in more than one charged particle in the final state, with one of them a pion detected by the TOF Spectrometer, and one of the others a particle detected by the VETO counter. The fact that the most forward angles were associated with the largest background is consistent with the

most forward angle yielding the largest discrepancy. This is also consistent with the abnormally large correction required for the empty target runs where the yield is almost solely from reactions on A>4 nuclei. Since the VETO correction technique was less reliable for these single-arm runs, only the Poisson correction scheme was used in that case. Such effects were *not* a concern for the two-arm runs, since in that case the backgrounds were very much lower, and the coincidence requirement between the pion and proton arms severely restricted the phase space available for background reactions yielding another charged particle with a trajectory intercepting the VETO counter.

C. Yield Extraction

The πp scattering yield at the pion scattering angle specific to a particular TOF spectrometer arm, $Y(T_\pi, \theta_{cm})$, for a given number of incident pions onto the target, N_π, was obtained by accumulating π2–P1 TOF difference events in the two-arm coincidence case, or by the π2 TOF events in the single-arm case. The desired πp scattering yield $Y(T_\pi,\theta)$ in Eq. 2 was obtained by subtracting an appropriately normalized background yield from the foreground, as the foreground yield contained contributions from both πp scattering on the hydrogen nuclei as well as other pion scattering reactions on the surrounding material which managed to satisfy the kinematical and geometrical constraints of the TOF spectrometer. Noting that the incident pion kinetic energies in the foreground and background runs were within 0.5 MeV in all cases, the πp scattering yield was determined from:

$$\begin{aligned} Y &= Y^{fg} - \left(\frac{N_\pi^{fg}}{N_\pi^{bg}} \cdot \frac{\Delta\Omega^{fg}}{\Delta\Omega^{bg}} \cdot \frac{\epsilon^{fg}}{\epsilon^{bg}} \cdot \frac{\cos\theta_{tgt}^{bg}}{\cos\theta_{tgt}^{fg}} \cdot \frac{N_{back}^{fg}}{N_{back}^{bg}} \right) \cdot Y_{back}^{bg} \\ &= Y_{fg} - \kappa \cdot Y_{back}^{bg} \end{aligned} \tag{6}$$

where $Y^{fg,bg}$ are the yields, $\epsilon^{fg,bg}$ the efficiencies, $N_\pi^{fg,bg}$ the number of incident pions, $N_{tgt}^{fg,bg}$ the areal target densities, $\Delta\Omega^{fg,bg}$ the solid angles, and $\cos\theta_{tgt}^{fg,bg}$ the target angles of the foreground and background targets.

Apart from the obvious dependence on target and beam, the foreground/background normalization factor, $\kappa(T_\pi, \theta_\pi)$, also depended on the pion angle. This dependence, due to the fact that the effective solid angle ($\Delta\Omega_{eff}$) differed (<1%) between the foreground and background targets, arose mostly because of different proton multiple scattering and/or pion and proton hadronic interaction losses in the two targets. The differences in the foreground and background solid angles for the two-arm coincidence setups could be reliably determined by the Monte Carlo simulation. Also, the particular value of κ used in the cross section calculations also depended on which multiple pion correction scheme (Poisson or VETO) was used, since they used different beam corrections.

For the two-arm coincidence technique, the foreground TOF difference peaks were narrow Gaussians with $\sigma \approx 300$ps. Most of the observed background under the foreground peak stemmed from pion quasi-elastic scattering from protons bound in heavier nuclei (mostly carbon) in the target region. This background was almost negligible for the smaller angles at 141 MeV, and reached a maximum level of about 7% for 218 MeV π^+p reactions in the CH_2 target at backward angles, as illustrated in Fig. 4. The final πp scattering yield was determined using wide (several σ) gates placed around the relevant spectra.

For the single–arm runs, the candidate π^+p scattering events were identified by the TOF difference between the π2 counter and the BEAM coincidence. Without the proton arm coincidences to discriminate against $\pi^+ + A \rightarrow \pi^+ + p + X$ quasi two–body events, pion quasi-elastic scattering and absorption on carbon contributed much larger backgrounds than in the two-arm runs. Although the timing resolution was adequate for separating pions from all but the fastest protons, the elastically and quasi–elastically scattered pions on carbon had very similar velocities to those from π^+p and so could not be separated except via a background subtraction. Figure 5 is an example of such a π2 timing spectrum at the most forward angle (20^0). As for the two-arm case, the foreground/background normalization factor was determined using Eq. 6. However, in the single-arm setup, the pions scattered in the full LH_2 target could *rescatter* in the surrounding target material (e.g., vacuum vessel, target ring) with the resulting final state pions or protons detected by the pion arms. This served to *enhance* the pion arm acceptance when the target was full relative to when it was empty. The added acceptance due to pion rescattering was determined by Monte Carlo simulation as outlined in Appendix A. The uncertainty in the net yield arising from the uncertainty in the normalization factor (from the counting statistics and the uncertainty in the relative target angle between foreground and background runs) was added in quadrature to the other statistical uncertainties. Despite the sizable backgrounds, the foreground–background subtraction resulted in a clean π^+p yield peak. An estimated 0.2±0.2% residual proton background (from the adjacent peak) was subtracted from the yields. Since the positions of the background peaks were often a few channels different from those of the foreground (due to small energy loss differences, timing drifts), the peaks were shifted appropriately before subtraction. In practice, such shifts made no statistical difference to the yields. The

extracted net yields were defined by a software gate placed around the π^+p peak. Slightly wider/narrower gates were used to check the sensitivity to the cut placement, and any differences were included in the overall statistical uncertainty.

1. Yields and Multiple Pion Correction

When dealing with the multiple pion events, due care had to be directed to the yield definition as well as to the beam normalization. In the Poisson correction scheme, the number of incident pions detected by the in–beam counters was *increased* by the factor in Eq. 4 to account for the multiple pion events. In this scheme, the π2-P1 TOF difference spectra included contributions from both single and multiple pion BEAM events, so no additional constraints needed to be applied to the yield spectra.

In the VETO correction scheme, a multiple pion event was identified by a particle hitting the VETO paddle at the same time as detection of a $\Pi\cdot$P coincidence in one of the TOF spectrometer arms. These events were then removed from the π2-P1 TOF difference spectra, resulting in a yield corresponding to only single–pion BEAM events. Correcting the resulting incident beam N_π for these rejected events using Eq. 5 resulted in cross–section values appropriate to single–pion beam events. In this (VETO) correction scheme, however, two special cases had to be considered, one where an event was vetoed but shouldn't have been, and vice versa.

In the first case, the extra particle(s) in the beam bursts could have been muons or electrons, which passed through the target and hit the VETO counter, while a pion in the same burst caused the $\Pi\cdot$P event. Although these πp events were rejected using the VETO cut, the incident BEAM count was also corrected for such events, so the effect cancels, the net result being simply a loss of statistics.

In the second case, where two (or more) pions were incident on the target in a beam burst, with one causing a $\Pi\cdot$P event, and the other continuing on to the VETO paddle, the latter pion could have interacted (e.g. decayed) prior to reaching the VETO counter with the interaction products (e.g., decay muon) *escaping* detection by the VETO. Here, the events should have been rejected but were not. Results from GEANT simulations showed that of the beam pions traversing the target, only about 6% failed to cause a VETO hit by either the pion or its decay muon. Thus for a typical 3% multiple pion correction, only about 0.2% of the events should have been identified as multiple pion events, but were not, a small effect consistent with observation.

IV. RESULTS

The many systematic checks that were performed to test our determinations of the effective solid angles, target thicknesses, and beam normalization (as illustrated in Figs. 7, 10, 11, 13, 17), indicated that the system was well understood. In all cases the test results were well within the normalization uncertainties ascribed to them. In fact, for the case of the LH_2 target angle, the test data (along with the overlapping π^+p single–arm and two–arm data) was *essential* to help determine the magnitude of the systematic angle offset and to estimate its uncertainty.

Both single–arm and two–arm π^+p scattering data were obtained at 141.2, 168.8, and 218.1 MeV, as shown in Figs. 18, 19, and 20. In general the agreement between the single– and two–arm results in their angular region of overlap is excellent. The Set "B" π^+p scattering data were obtained at 141.2, 168.8, 218.1, and 267.3 MeV (as shown in Figs. 18, 19, 20 and 21) in the middle of the experimental running period, and necessitated removing and repositioning the TOF Spectrometer pion arms. The target angle was slightly different as well, 50.6° compared to 53.6°. The excellent agreement of the Set B data with the corresponding Set A data provides additional confirmation of the positional accuracy of the counter arms and the accuracy of our solid angle determinations.

Data were obtained using both solid and liquid targets for π^+p scattering in the two–arm configuration at 141.2, 168.8, 193.2 and 218.1 MeV and for π^-p scattering at 141.2, 168.8 and 193.2 MeV (as shown in Figs. 18, 19, and 20). In general, the agreement between the solid and liquid target results is good, within the ascribed normalization uncertainties, *except* at 193.2 MeV, where the solid target results were consistently larger than the liquid target results for both π^+p and π^-p. Neither the beam normalization constants (f^π, f_S, etc.), the foreground and background yields, the effective solid angles, nor the beam energy in these sets appear out of line with respect to the adjacent energies, so the source of the discrepancy is unclear. Possible reasons include erroneous settings of the CH_2 target angles (which were readjusted for each energy) and/or the momentum selecting slits, which if mistakenly adjusted off centre, could cause the central beam energy to shift. Neither of these would have caused any change in our diagnostics or our data and thus would have escaped detection. Since at every other energy the agreement among the various experimental configurations is good, the normalization uncertainties for just these four data sets at 193.2 MeV were increased, to

2% for the two π^-p runs, and 2.5% for the two π^+p runs, to bring them into agreement at the limit of their 1σ normalization uncertainties.

A. The Absolute Differential Cross Sections

The final results for the π^+p and π^-p elastic absolute differential cross sections in the centre–of–mass system are listed in Tables III through IX. The uncertainties quoted are the usual 1σ values. Common uncertainties such as those associated with beam energy and normalization are *not* included in the errors associated with each data point, but are listed separately. All the data of each type were obtained from runs characterized by a fixed experimental configuration (i.e. beam rate, target angle, etc.), except for the 168.8 MeV π^+p LH_2 and CH_2 two-arm results, which are weighted averages of runs taken with three different beam rates, and three different target thicknesses, respectively. The justification for this averaging is provided by Figs. 11 and 17, which indicated *no* systematic dependence of the cross-section on these parameters. The final cross sections had statistical uncertainties of ∼1-1.5% for π^+p and ∼1.5-2% for π^-p, each with ∼1-1.5% normalization uncertainties.

1. Uncertainties in the Absolute Normalization

The normalization uncertainties quoted in the tables are based on the following considerations:

- **Target Angle, $\cos\theta_{\mathbf{tgt}}$:** $\pm0.4^\circ$(zero offset)$\pm0.2^\circ$(reproducibility) for the LH_2 target, corresponding to a ±1.1 (1.0)% uncertainty in $\cos\theta_{\rm tgt}$ for $\theta_{\rm tgt}$ = 53.6 (50.6)° in the two-arm setups, and ±0.6% for $\theta_{\rm tgt}$ = -39.4^0 (single-arm setup). For the CH_2 targets, we estimate an uncertainty of $\pm0.25^0$ corresponding to $\delta\cos\theta_{\rm tgt}$= 0.6%. These estimates are based on the results discussed in Sec. II C 1.
- **Multiple Pion Correction, f_S:** A conservative estimate of ±10% is ascribed to the value of $|1-f_S|$ determined for each run, a value justified by the excellent agreement exhibited by the results discussed in section III B 6 and shown in Fig. 17.
- **Pion Fraction, f_π:** For the π^+p data the uncertainties ranged from ±0.3% at 141.1 MeV to ±0.1% at 267.2 MeV, as inferred from direct measurements during the phase-restricted beam operation described in Sec. III B 2 and shown in Fig. 13. For the π^-p data, the uncertainties ranged from 0.9% at 141.1 MeV to 0.3% at 267.2 MeV. Up to 193 MeV, the uncertainties are associated with the fits to the TCAP spectra as discussed in Sec. III B 2.
- **Pion Decay, f_D:** ±0.2% in all cases, since the results of the GEANT and REVMOC simulations used to generate these corrections agreed to <0.1%. Another 0.1% was added for the uncertainty in the contribution from pion decay within the channel as discussed in Sec. III B 3.
- **Hadronic Interaction Loss, f_L:** This uncertainty was estimated to be 15% of the calculated loss to the centre of the target, varying from 0.3% for 168.8 MeV π^+p on the LH_2 targets, to 0.1% for 193.2 MeV π^-p on the 2 mm CH_2 target.
- **Target Proton Density, $N_{\mathbf{prot}}$:** The uncertainty in the proton density of the LH_2 target, ±0.5%, was estimated from the vapour bulb measurements conducted during the experiment (see section II C). The uncertainty in the proton density of the CH_2 targets was ±1% , as measured by chemical analysis by a commercial laboratory [48] (see Sec. II C).
- **Beam and Computer Live Time, B and f_{LT}:** The uncertainties in both these quantities were negligible, <0.1%, since the particle counting was done with several independent scaler modules with no discrepancies observed. The live-time f_{LT} was 0.98 or better for the data presented in the tables.

All of the normalization uncertainties outlined above were combined in quadrature to yield the values quoted in the tables. As an example, Table II shows the uncertainties and their sum for the 168.8 MeV data.

2. Angle–Dependent Uncertainties

The experimental uncertainties which depended on the pion scattering angle are the counting statistics in the foreground and background runs, the statistics in the Monte Carlo determinations of the solid angles, the uncertainties in the hadronic loss corrections of the scattered pions and recoil protons, and the uncertainty in the distance from the relevant $\pi 2$ counter to the target centre ($\pm 0.5\%$ corresponding to ± 3 mm).

The uncertainty in the net yield Y given by Eq. 6 is $\Delta Y = \sqrt{(\delta Y^{fg})^2 + (\kappa \cdot Y^{bg}_{back})^2 \cdot \left((\frac{\delta\kappa}{\kappa})^2 + (\frac{\delta Y^{bg}_{back}}{Y^{bg}_{back}})^2\right)}$ where the uncertainties in the foreground and background yields are Poisson distributed and the foreground/background normalization uncertainty $\delta\kappa$ arises mainly from the target angle uncertainties in the foreground and background runs. In practice, the second term involving κ was negligible in the two-arm measurements where the backgrounds were very small, but it was non–negligible in the single-arm runs, where backgrounds were typically 25% (but even up to 50% at 20^0) of the foreground yields. Also, for the single-arm runs, there was some uncertainty in the yields arising from the placement of the software cuts, uncertainties which were added in quadrature to the other uncertainties. In practice, these variations were never larger than half of the statistical uncertainties. The hadronic loss uncertainty was estimated to be 10% of the actual loss suffered by the pions and protons. The final "statistical" uncertainties were obtained by summing in quadrature all these separate components. Reference [33] provides a sample calculation of all solid angle corrections.

3. Radiative Corrections

In experiments utilizing magnetic spectrometers to detect scattered charged particles, the fraction of events lying outside the spectrometer energy acceptance due to bremsstrahlung energy loss would have to be considered. In our measurements, however, the times–of–flight of the pions and protons were measured, not the energy, and so energy losses would manifest themselves as tails in the timing distributions. No such tails were observed in any of our spectra. As the cross section for the bremsstrahlung process ($\pi p \rightarrow \pi p \gamma$) is known to be very small ($<<0.1$ mb/sr) [57], any radiative corrections would have been negligible compared to the other uncertainties characterizing the experiment. Consequently, no radiative corrections were applied to the data.

V. DISCUSSION

In Figs. 18 through 21, the cross section results are shown as ratios to the Karlsruhe–Helsinki KH80 PWA solution [17]. Also shown are the results of the last published PWA from the V.P.I. group, SM95 [19] and the data of Bussey et al. [26], Brack et al. [28,29], and Sadler et al. [30], all plotted as ratios to KH80 at their respective energies. The use of such ratios enables meaningful comparisons since the data sets were measured at somewhat different energies, and also highlights differences between the data sets which would not be visible on an absolute scale.

Prior to this work, the results of Bussey et al. [26] constituted the only comprehensive set of differential cross sections for energies spanning the Δ resonance. The two previous TRIUMF experiments of Brack et al. [28,29] covered a range of energies up to $\sim$139 MeV, whereas those of the LAMPF group of Sadler et al. [30] were at higher energies, extending down to 263 MeV, both of which overlap our energy range. Although there are also π^+p data up to 140 MeV by Ritchie et al [58], the 140 MeV data were not included in Fig. 18 for reasons of clarity[6]. Of particular interest are the results of Brack et al. which employed a spectrometer similar to that used in our experiment. Whereas their first experiment [28] used solid CH_2 targets in a πp two-arm coincidence configuration, their second [29] used an active scintillator target to detect the recoil proton. The pion arm scintillators used in their experiment were also different from ours.

Our lowest energy results agree within uncertainties with the earlier two-arm coincidence measurements of Brack et al. [28], although the latter are systematically lower than ours by 1–2%. The results of the forward angle active target experiment of Brack et al. [29] are also consistent with our data, although at the edge of the relative normalization uncertainty of about 3%. Our π^+p results at 141 MeV are also in good agreement with the data of Ritchie et al. [58] at 140 MeV. Our highest energy results at $\approx$267 MeV are completely consistent in both normalization and shape with

[6]Other data sets [25] also were excluded in figures 18 through 21 due to the few energies covered and the large error bars associated with the data, which limits their impact in partial wave analyses.

those of Sadler, et al. [30] which have 3% and 5% normalization uncertainties for the π^+p and π^-p data respectively. Comparison of our data with those of Bussey et al. yield a mixed picture[7]. Above the resonance, there is consistency within the stated uncertainties. However at energies below the resonance peak, our results are systematically lower than theirs, particularly for π^-p, with the largest disagreement occurring at 141 MeV. It is noteworthy that at the lower energies, the Bussey et al. [26] cross-sections are systematically larger than the Brack et al. [28,29] results, with our data slightly below half-way between the two sets at 141 MeV. Also, our data have better statistical precision than any of these other data sets.

Our results are systematically lower than, and in clear disagreement with, the KH80 PWA solution at energies below the resonance, though there is better agreement with KH80 above the resonance. Our results agree rather well with the predictions of the SM95 solution at all energies, even though our data were not used in the SM95 fitting. Note that the Bussey et al. [26] data were included in the KH80 database with *no* normalization uncertainties, but were assigned 5% normalization uncertainties in the SM95 database (compared to the 0% quoted [26] and the 1% provided subsequently [32]) in order to resolve an inconsistency between the single-energy and global fits in the SM95 solution. The increased uncertainty, hence reduced weight, of the Bussey et al., data resulted in a solution more consistent with the global database. The generally good agreement between our results and the SM95 predictions demonstrate that our results are more compatible with the global database in the vicinity of the Delta resonance than were the previous measurements. In addition, we have provided data with superior statistical precision. The precision is such that shape differences due to the difference in the small D-waves between the SM95 and KH80 solutions are clearly seen in the data at the highest energies.

Although the full impact of our data can only be appreciated after a new global PWA fit[8], the consistency between our data and the SM95 PWA solution permit some preliminary observations. The SM95 solution provides a good fit to the total cross section results of Pedroni et al. [31], but much less so to those of Carter et al. [27] (which are larger than Pedroni on the left-wing of the resonance), so our data support the former data set. Our data also support the value of the πNN coupling constant derived from the SM95 solution, f^2 $\sim$0.076, over that of KH80 (0.079), a result which can be traced to the smaller mass and narrower width of the Delta resonance in the SM95 solution compared to KH80. The lower value of the coupling constant is known to resolve long standing inconsistencies in the Goldberger-Treiman discrepancy [8] and Dashen-Weinstein sum rule [10,12,13]. The πN sigma term from SM95 and subsequent preliminary solutions which include our data [60] seem to indicate a sigma term *larger* than the canonical result [15], thereby *increasing* the discrepancy with the theoretical result [16]. However, since the sigma term is a very difficult quantity to extract from the πN data, definitive conclusions cannot be reached at this time.

A. Concluding Remarks

The primary goal of our experiment was to provide absolute differential cross section data with small and *reliable* uncertainties at energies spanning the Δ resonance. In addition, the results of many test measurements proved invaluable in elucidating the nature of systematic errors which were subsequently corrected or accounted for in the uncertainties. The satisfying internal consistency of our results demonstrates that our goal of obtaining reliable estimates of systematic uncertainties was successfully attained. It also demonstrates that the techniques employed in this experiment and shared by the previous work of Brack et al. [28,29,49], such as the use of solid targets, were reliable, despite criticisms to the contrary (see e.g. [61]).

These data resolve a long standing controversy regarding the inconsistency of cross section values around the Delta resonance with those at lower energies. Consequently, inclusion of the results of this work will result in a more consistent database than was previously available. As a result of the improved consistency in the database and the increased precision of these data over previous results, more accurate and reliable determinations of the πNN coupling constant and πN sigma term can be expected.

---

[7]We refer to the $\approx$1% normalization uncertainties ascribed to the Bussey data after publication [32], and not the larger 5% value adopted in the SM95 analysis [19]. No value was quoted in the original paper [26].

[8]Preliminary solutions which include our data can be found at the SAID site [59]

VI. ACKNOWLEDGEMENTS

The authors wish to acknowledge the National Science and Engineering Council of Canada for financial support, the TRIUMF cryogenic target and cyclotron operation groups for their invaluable assistance, and PNPI Gatchina for providing their surface barrier detectors. M.M.P. acknowledges support by the Wescott Fellowship and E.W. Vogt, and thanks G. Stinson and R.A. Pavan for assistance with the REVMOC and TRANSPORT beam transport codes. I.S. acknowledges the hospitality of TRIUMF, the support of E.W. Vogt, and the NATO Collaborative Research Grant #921155U.

APPENDIX A: HADRONIC INTERACTION CORRECTIONS TO THE SOLID ANGLES

The GEANT [54] simulations described in Sec. III A included all the geometrical constraints and physical processes that could affect the solid angle, except for pion or proton inelastic interactions with nuclei, for which GEANT was found to be unreliable in the energy region involved in this experiment[9]. Hadronic elastic and quasi-elastic interactions were included to simulate pion hadronic rescattering into the pion arms from the cryostat vessel and target ring. However, as the hadronic rescattering corrections were never large, but only up to 1% in the forward angle single arm runs, even a large uncertainty there would not increase the overall solid angle uncertainty appreciably. In practice, an additional uncertainty of 33% of the additional correction was applied in those cases.

A specific test was carried out to check these rescattering corrections. In this test, the proton arms were removed from the EVENT coincidence. Though now in single–arm detection mode, the proton arm information was still recorded, so both single-arm and two-arm yields were obtained *simultaneously*. Comparison of the single-arm and two-arm cross-sections *without* including pion hadronic rescattering in the vacuum vessel and target ring showed that the single–arm results were systematically larger than the two–arm results by about 1 to 4% (Fig. 22). However, including the additional pion hadronic rescattering contribution brought the two into agreement. As an additional check, another empirical method was used to account for the additional rescattering acceptance (see Ref. [49]). The ratio between a full and empty target run of counts in a software box placed around the background pulse–height versus timing spectrum (e.g. Fig. 5) was used for the foreground/background normalization constant (see Eq. 6). Additional contributions to empty target background from pion *quasi*-elastic rescattering in the vacuum vessel appear in the background software box, and this increase closely mimics the increase of the *elastic* rescattering in the true yield box. Uncertainties arise from the counting statistics in the software boxes, and from the fact that the quasi-elastic rescattering contribution does not necessarily match exactly the elastic contribution. The additional uncertainties are not expected to be bigger than about a third of the total rescattering correction. The results from this method also are shown in Fig. 22, and are seen to agree with the simulated hadronic rescattering corrections.

Unlike the pion (quasi-)elastic rescattering corrections, the hadronic inelastic interaction *losses* of the pions and protons through the target, air (and for pions, the $\pi 1$ counter) on their way to their respective counters were relatively large (up to 7%). A program was developed to calculate these losses, since it was found that the GEANT simulations were unreliable. Consequently, the hadronic losses were determined using the program and then applied *post priori* to the GEANT solid angle results calculated with hadronic inelastic interaction disabled. Details, including a sample loss calculation, can be found in Ref. [33].

[1] J. Gasser and H. Leutwyler, Ann. Phys. **158** 142 (1984).
[2] V. Bernard, N. Kaiser, and Ulf-G. Meißner, Int. J. Mod. Phys. E **4** 193 (1995).
[3] M.E. Sainio, in πN Newsletter No.13, *Proceedings of the Seventh International Symposium on Meson Nucleon Scattering and the Structure of the Nucleon, Vancouver, Canada, 1997*, edited by D. Drechsel, G. Höhler, W. Kluge, H. Leutwyler, B.M.K. Nefkens, H.-M. Staudenmaier (UCLA, IEKP-Karlsruhe, 1997), p. 144 ; in *Chiral Dynamics, Theory and Experiment Workshop, M.I.T., Cambridge, MA, U.S.A. 1994*, edited by A.M. Bernstein, B.R. Holstein (Springer-Verlag, 1995).

[9] As GEANT v3.21 was designed as a simulation tool for high energy physics, many of the approximations used in the hadronic interaction routines are not appropriate at low energies.

[4] T.P. Cheng and Roger Dashen, Phys. Rev. Lett. **26** 594 (1971).
[5] J. Gasser, H. Leutwyler, and M. Sainio, Phys. Lett. B **253**, 252 (1991) ; *ibid* **253**, 260 (1991).
[6] J.J. deSwart, M.C.M. Rentmeester, R.G.E. Timmermans, in πN Newsletter No.13, *Proceedings of the Seventh International Symposium on Meson Nucleon Scattering and the Structure of the Nucleon, Vancouver, Canada, 1997*, edited by D. Drechsel, G. Höhler, W. Kluge, H. Leutwyler, B.M.K. Nefkens, H.-M. Staudenmaier (UCLA, IEKP-Karlsruhe, 1997), p. 96.
[7] J. Gasser, M.E. Sainio, and A. Svarc, Nucl. Phys. B**307** 779 (1988).
[8] G.L. Goldberger and S.B. Treiman, Phys. Rev. **111**, 354 (1958).
[9] H. Pagels, Phys. Rep. **16**, No.5, 219 (1975).
[10] R. Dashen and M. Weinstein, Phys. Rev. **188** 2330 (1969).
[11] C.A. Dominguez, Riv. del Nuovo Cimento **8** N.6, 1 (1985).
[12] N. Fuchs, H. Sazdjian, and J. Stern, Phys. Lett. B **238**, 380 (1990).
[13] J. Goity, et al., Los Alamos preprint hep-ph/9901374.
[14] R.L. Jaffe, C.L. Korpa, Comments Nucl. Part. Phys. **17** 163 (1987).
[15] R. Koch, Z. Phys. C **15**, 161 (1982).
[16] J. Gasser, Ann. Phys. **136**, 62 (1981) ; J. Gasser and H. Leutwyler, Phys. Rep. **87** 77 (1982).
[17] R. Koch and E. Pietarinen, Nucl. Phys. A **336**, 331 (1980).
[18] T.E.O. Ericson, et al., Phys. Rev. Lett. **75** 1046 (1995).
[19] R.A. Arndt, I.I. Strakovsky, R.L. Workman, and M.M. Pavan, Phys. Rev. C **52**, 2120 (1995).
[20] R.G.E. Timmermans, in πN Newsletter No.13, *Proceedings of the Seventh International Symposium on Meson Nucleon Scattering and the Structure of the Nucleon, Vancouver, Canada, 1997*, edited by D. Drechsel, G. Höhler, W. Kluge, H. Leutwyler, B.M.K. Nefkens, H.-M. Staudenmaier (UCLA, IEKP-Karlsruhe, 1997), p. 80.
[21] R. Machleidt and F. Sammarruca, Phys. Rev. Lett. **66**, 564 (1991).
[22] R. Machleidt and G.Q. Li, in πN Newsletter No.9, *Proceedings of the 5^{th} International Symposium on Meson-Nucleon Physics and the Structure of the Nucleon, Boulder, Colorado, 1993*, Vol.2, edited by G. Höhler, W. Kluge, B.M.K. Nefkens, M. Clajus (UCLA, IEKP-Karlsruhe, 1994).
[23] Many articles documenting these discrepancies can be found in the "πN Newsletter" series, volumes 1-15, published by UCLA and IEKP-Karlsruhe.
[24] G. Höhler, *Pion Nucleon Scattering*, Landolt–Bornstein, Group 1, V.9:B:2, edited by H. Schopper (Springer, Berlin 1983).
[25] Ottermann et al., Phys. Rev. C **32** 928 (1985), Troka et al., Phys. Rev. **144** 1115 (1966), and B.M.K. Nefkens et al., Phys. Rev. D **18** 3911 (1978).
[26] P.J. Bussey, J. R. Carter, D.R. Dance, D.V. Bugg, A.A. Carter, and A.M. Smith, Nucl. Phys. B **58**, 363 (1973).
[27] A.A. Carter, J.R. Williams, D.V. Bugg, P.J. Bussey, D.R. Dance, Nucl. Phys. B **26**, 445 (1971).
[28] J.T. Brack, et al., Phys. Rev. C **34**, 1771 (1986).
[29] J.T. Brack, et al., Phys. Rev. C **51**, 929 (1995).
[30] M.E. Sadler, W. J. Briscoe, D.H. Fitzgerald, B.M.K. Nefkens, and C.J. Seftor, Phys. Rev. D **35**, 2718 (1987).
[31] E. Pedroni, et al., Nucl. Phys. A **300**, 321 (1978).
[32] The original paper [26] quotes no normalization uncertainties. The uncertainties were subsequently updated to $\approx$0.5-1% in correspondence to R.A. Arndt from D.V. Bugg. R.A. Arndt (private communication).
[33] M.M. Pavan, Ph.D. Thesis, University of British Columbia, 1995 (unpublished). Note that the results from this work supersedes those from the thesis. Copies available upon request from the corresponding author.
[34] M. Sevior, et al., Phys. Rev. C **40**, 2780 (1989).
[35] D.V. Bugg, in πN Newsletter No.2, edited by G. Höhler, W. Kluge, B.M.K. Nefkens, 1990 (unpublished).
[36] The transistorized tubes and bases were proprietary designs of the nuclear physics group at the University of Regina, Saskatchewan.
[37] TRIUMF Users' Handbook, July 1987 (unpublished).
[38] D.F. Ottewell, C. Oram, TRIUMF Memo to M11 Users' 85-F-EF/GEN, 1985 (unpublished)
[39] C. Joram, Universität Karlsruhe (private communication). After noticing a similar effect, this group pointed out to us the references which explained the discrepancy.
[40] M. Martini, et al. IEEE Transactions on Nuclear Science, **NS–22** (1975).
[41] W. Kemper, J.D. Fox, Nucl. Instrum. Methods **105**, 333 (1972).
[42] R. Langley, Nucl. Instrum. Methods **113**, 109 (1973).
[43] D.S. Haynes, K.W. Kemper, and N.R. Fletcher, Phys. Rev. C **5**, 5 (1972).
[44] *Semiconductor Detectors*, edited by G. Bertollini, A. Coche (North Holland, Amsterdam 1968).
[45] T.R. King, et al., Nucl. Instrum. Methods **88**, 17 (1970).
[46] LOSSPROG, An Energy Loss Program. L.G. Greeniaus, University of Alberta
[47] Result is based on average of several measurements on a single π2 counter made during the course of TRIUMF Experiment E322 [28]. J.T. Brack (private communication)
[48] J.T. Brack, Ph.D. Thesis, University of Colorado, Boulder, 1989 (unpublished).
[49] J.T. Brack, J.J. Kraushaar, D.J. Rilett, R.A. Ristinen, D.F. Ottewell, G.R. Smith, R.G. Jeppensen, and N.R. Stevenson,

Phys. Rev. C **38**, 2427 (1988).
[50] W. Kelner, TRIUMF Targets Group (private communication).
[51] R.J. Tapper, Rutherford High Energy Laboratory, National Institute for Research in Nuclear Science, Preprint NIRL/R/95, March 1965 (unpublished).
[52] The silicon counters were supplied by the Petersburg Nuclear Physics Institute.
[53] VDACS Data Acquisition System. Users' manual and related documentation available from the TRIUMF Computing Group, or on the World–Wide–Web at http://www.triumf.ca/dagroup.html
[54] GEANT3 Version 3.21, High energy physics detector description and physical process Monte Carlo simulation program, CERN Applications Software Group (Simulation Section), CERN, Geneva, 1993.
[55] REVMOC, A Monte Carlo Beam Transport Program. Users' manual available from the TRIUMF Computing Group, or on the World–Wide–Web at http://www.triumf.ca/compserv.html
[56] G.R. Smith, et al., Phys. Rev. C **38**, 240 (1988).
[57] R. Wittman, Phys. Rev. C **37**, 2075 (1988) ; L. Heller, et al. , Phys. Rev. C **35**, 718 (1987).
[58] B.G. Ritchie, et al,. Phys. Lett. B **125**, 128 (1983).
[59] **S**cattering **A**nalys**i**s **D**ialin program. Available via URL http://gwdac.phys.gwu.edu, or via SSH login at gwdac.phys.gwu.edu, username 'said'.
[60] M.M. Pavan, R.A. Arndt, I.I. Strakovsky, and R.L. Workman, in πN Newsletter No.15, *Proceedings of the 8th International Symposium on Meson-Nucleon Physics and the Structure of the Nucleon, Zuoz, Engadine, Switzerland, 1999*, edited by D. Drechsel, G. Höhler, W. Kluge, H. Leutwyler, B.M.K. Nefkens, and H-.M. Staudenmaier (UCLA, IEKP-Karlsruhe, 2000), p.118 ; Los Alamos eprint nucl-th/9912034.
[61] D.V. Bugg, in πN Newsletter No.3, edited by R.E. Cutkosky, G. Höhler, W. Kluge, B.M.K. Nefkens, 1991 (unpublished).

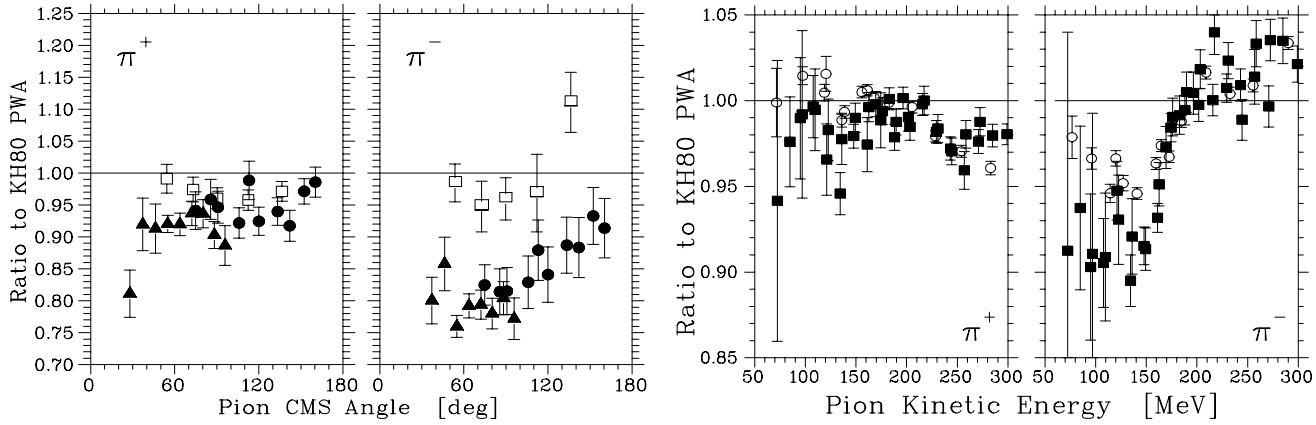

FIG. 1. **Left:** Differential cross sections near T_π =117 MeV of Bussey et al. [26] (open) versus Brack et al [28,29] (solid) plotted as a ratio to the KH80 PWA solution [17] at their respective energies. **Right:** Total cross sections as a function of energy showing the results of Carter et al. [27] (open) versus Pedroni et al. [31] (solid).

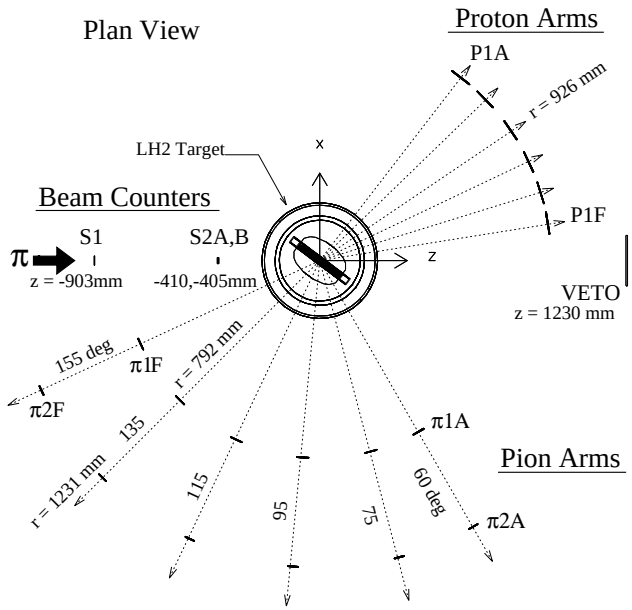

FIG. 2. Plan view of the TOF spectrometer, showing the distances between centrelines of the counters and target, and the pion arm angles for 'Set A'. Proton arm angles vary with energy (see text). The pion beam enters at centre left.

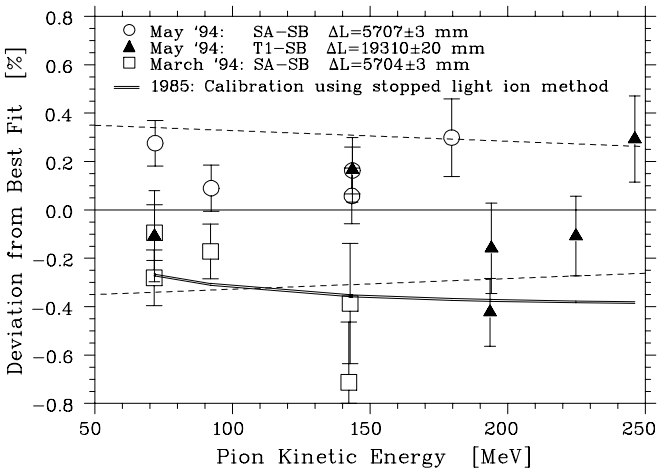

FIG. 3. Results from our pion channel energy calibration using the π-e TOF difference technique. The data points show the % deviation in kinetic energy from the resulting best-fit calibration. The dashed lines represent the estimated $\pm 0.2\%$ momentum uncertainty. Also shown is the calibration from the 1985 analysis [38], which used the technique of measuring the energy of light ions in the beam when stopped in a silicon counter.

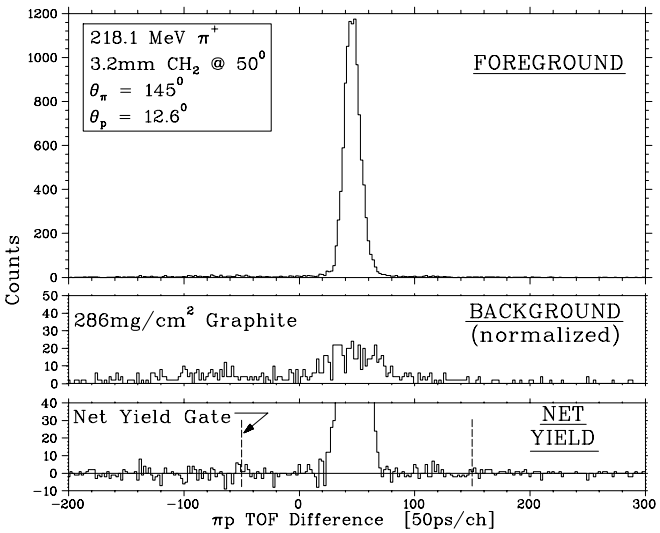

FIG. 4. Foreground, normalized background, and net πp TOF difference spectrum at 145^0 laboratory angle for 218 MeV π^+p on a 3.2 mm CH_2 target. This setting had the *worst* background–to–foreground ratio ($\approx$7%) of *all* the two–arm runs in the experiment (which were typically $\approx$1-3%). A software yield–defining gate is shown by the vertical dashed lines.

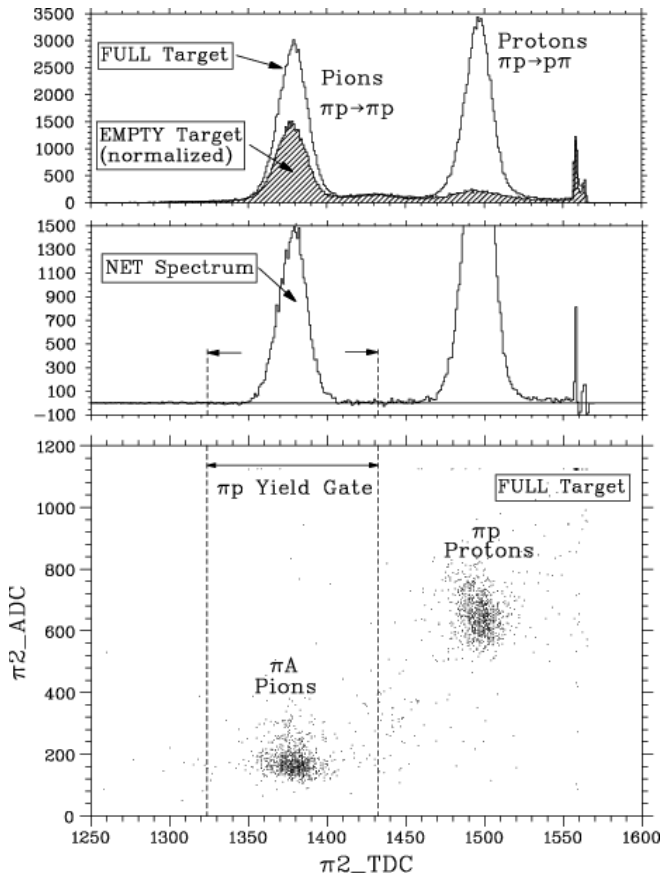

FIG. 5. **Top:** A $\pi 2$ timing spectrum (θ_π=20°) showing the software gate used to extract πp yield from a 169 MeV π^+p single–arm run. The background level was maximal here and decreased with larger angle. The protons shown, corresponding to backward going pions, were fast enough to satisfy the hardware EVENT timing requirement. **Bottom:** $\pi 2$ foreground pulse height versus timing spectrum, showing clear separation of pions and protons. The πp yield was defined using the one dimensional gate shown.

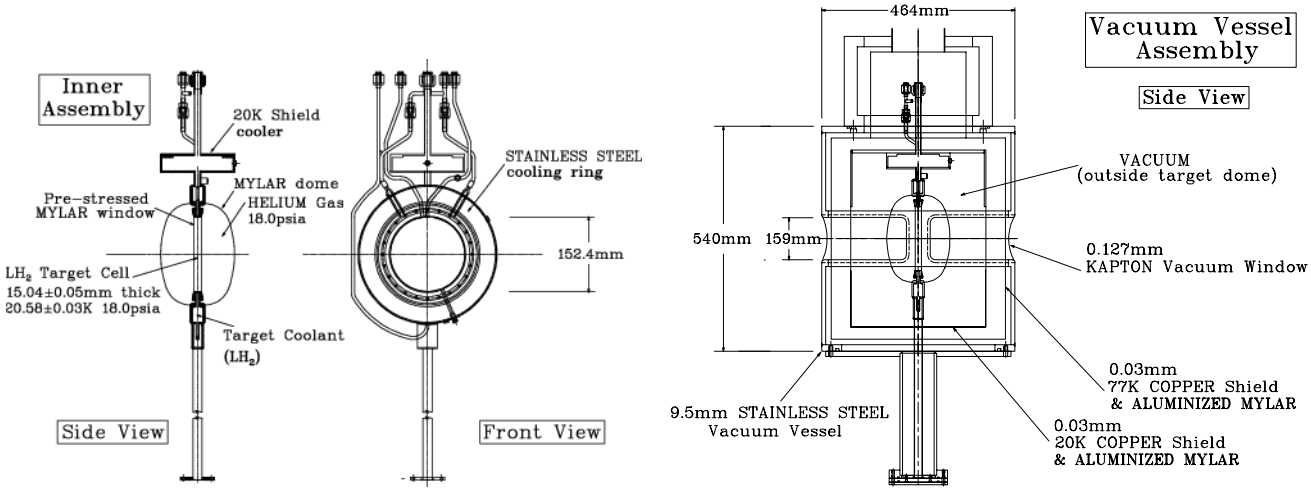

FIG. 6. **Left**: LH_2 target inner flask assembly, showing target dimensions and operating temperature and pressure. **Right**: Target assembly showing placement of target flask assembly within outer vacuum vessel.

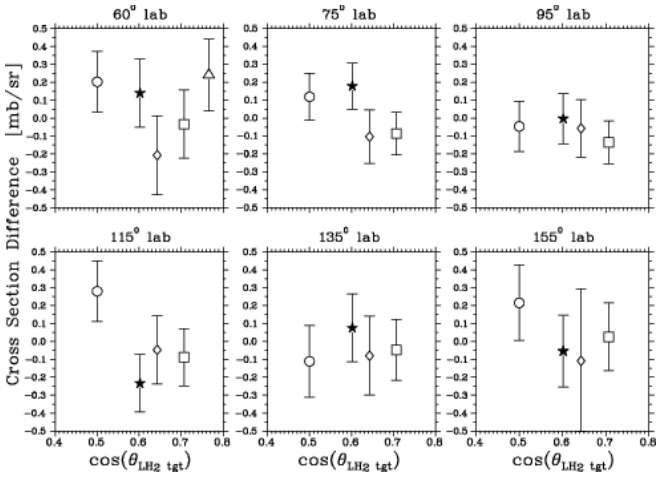

FIG. 7. Two–arm π^+p cross sections at 169 MeV taken with the LH_2 target at angles of 45.6°, 50.6°, 53.6°, and 60.6°. For θ_π=60° lab, there is an additional point at -39.4°. Each graph represents one pion detection arm. The (≈1.3%) uncertainties shown are statistical only. A target offset of +0.6°±0.4° was inferred from a combination of these results together with an independent target thickness measurement (Fig.8).

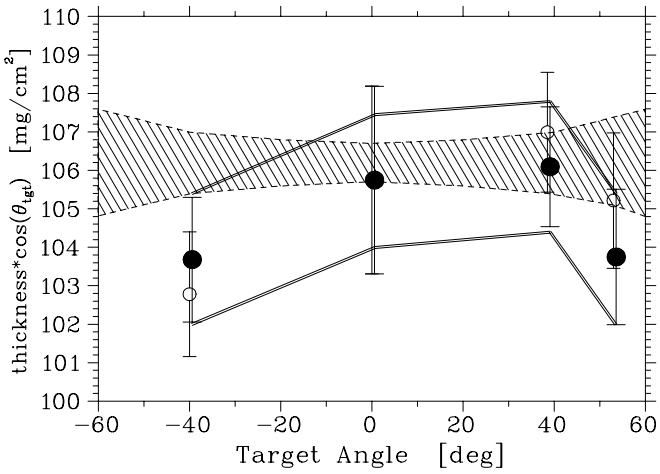

FIG. 8. Results from the two different LH_2 target thickness measurement methods. The solid (open) data points are the proton energy loss results including (ignoring) the effect of a 0.6^0 angular offset. The ±1.6% normalization error band does *not* include the contribution from the statistical errors. The hatched area represents the quoted target thickness uncertainty from our vapour bulb result (t_{tgt}= 106.2±0.5, Sec. II C) as a function of angle, combining the 0.5% thickness uncertainty with the $\pm 0.4^0$ zero–offset angle uncertainty.

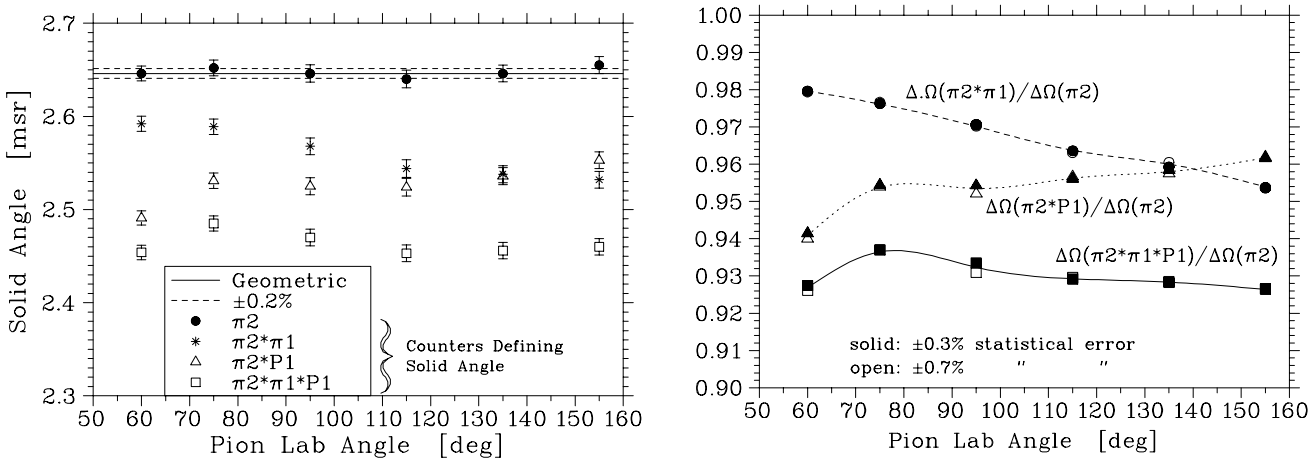

FIG. 9. **Left:** Results of a GEANT solid angle simulation for a 141 MeV π^+p run using a 2mm CH_2 target oriented at 53^0. No hadronic interaction losses are included at this stage. Note that the $\pi 2$ solid angle equals the geometric solid angle as expected. **Right:** Ratios of the simulated solid angles to the simulated $\pi 2$ solid angle, showing the equivalence of the high statistics simulation with the lower one used in the analysis (see text). Note that inclusion of the $\pi 1$ and $P1$ counters reduced the solid angle by only ≈7-8% from the geometric value. The lines merely serve to guide the eye.

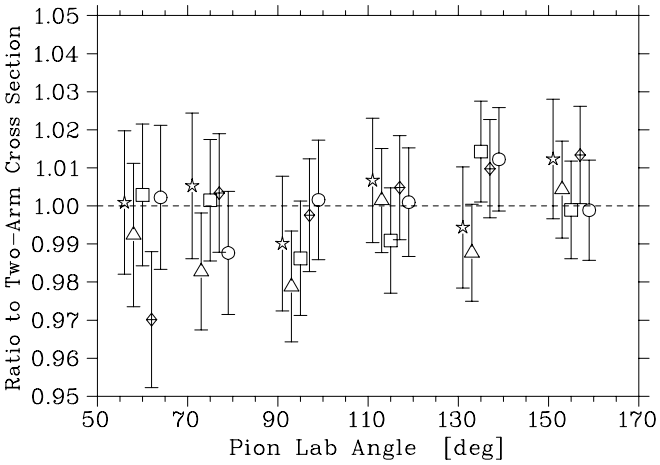

FIG. 10. π^+p cross section ratios to the normal two-arm value at 169 MeV using the LH_2 target, measured for various configurations at different times during the experiment. For clarity, the angles are offset from one another, and the uncertainties shown are statistical only. The boxes (crossed diamonds) refer to runs when the proton arm radius (angle) was shifted, the stars (circles) when the proton P1 (pion $\pi 1$) counter was removed from the coincidence, and the triangles when the beam momentum spread was increased to 3% (from 1%). These results demonstrate the insensitivity of our technique to such systematic effects.

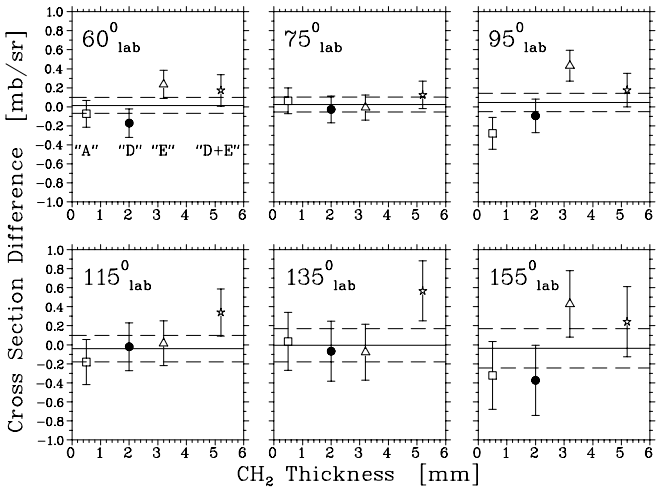

FIG. 11. π^+p cross section differences at 169 MeV for the two–arm setup using CH_2 targets of various thicknesses. The uncertainties shown are purely statistical. Not shown are normalization uncertainties dominated by the target proton density (1%) and the $\pm 0.2^0$ target angle error (0.5%). The horizontal solid and dashed lines represent the weighted average and uncertainty ($\approx$0.8%) for the three targets "A", "B", "D". The solid points are the data used for the final results at this energy. These results confirm the quoted 1.4% relative density uncertainty for these targets.

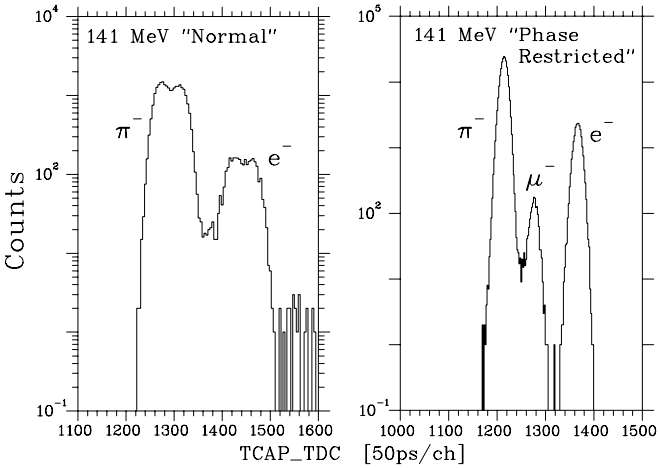

FIG. 12. **Left:** Normal pion beam time structure measured with respect to the TCAP probe as exhibited during a 141 MeV π^-p run. The electrons are clearly separated, but the muons are totally obscured under the pion and electron peaks. **Right:** TCAP time spectrum, obtained during a dedicated run using phase–restricted primary proton beam on the pion production target. In this case, the pions, muons, and electrons are all clearly distinguished.

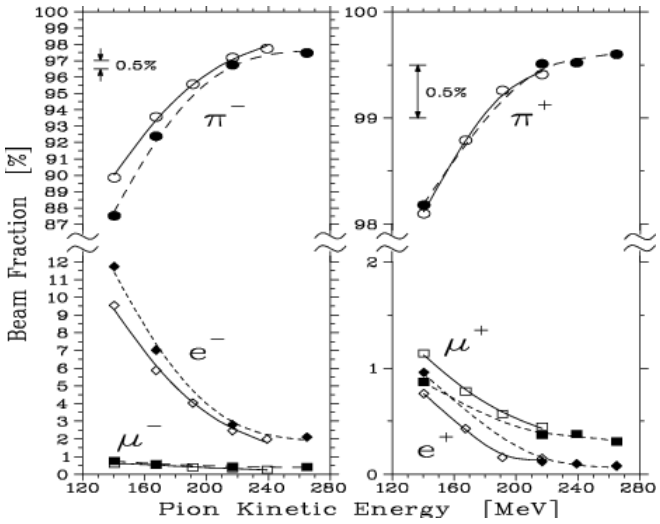

FIG. 13. Percentage of pions, muons, and electrons in the M11 beam as defined by the in–beam scintillators during two runs (run 1 open ; run 2 filled points) with phase-restricted primary proton beam. The differences between the series are due in part to changing electron contamination from different midplane slit settings (see text). The relative $\pi/(\pi+\mu)$ fraction is constant ($\leq$0.2% difference at 141 MeV) between the two series. The beam composition was found to be insensitive to typical drifts of the proton beam location on the production target. The lines merely serve to guide the eye.

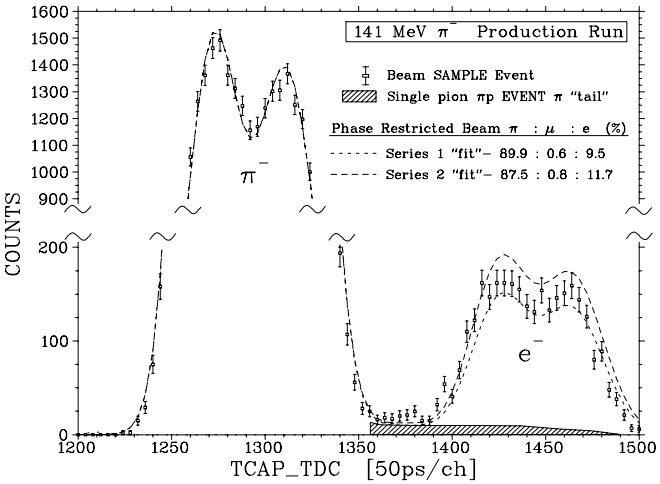

FIG. 14. Example of a beam sample TCAP timing spectrum taken during normal production running. Two Gaussians are fit to the pion peaks, and the electron and muon (obscured by the π and e peaks) contributions are estimated using the results obtained from the phase restricted beam runs. This technique was used to estimate f_π for the production runs. The tail to the pion timing distribution is inferred from true πp coincident events associated with only a single beam pion per bucket.

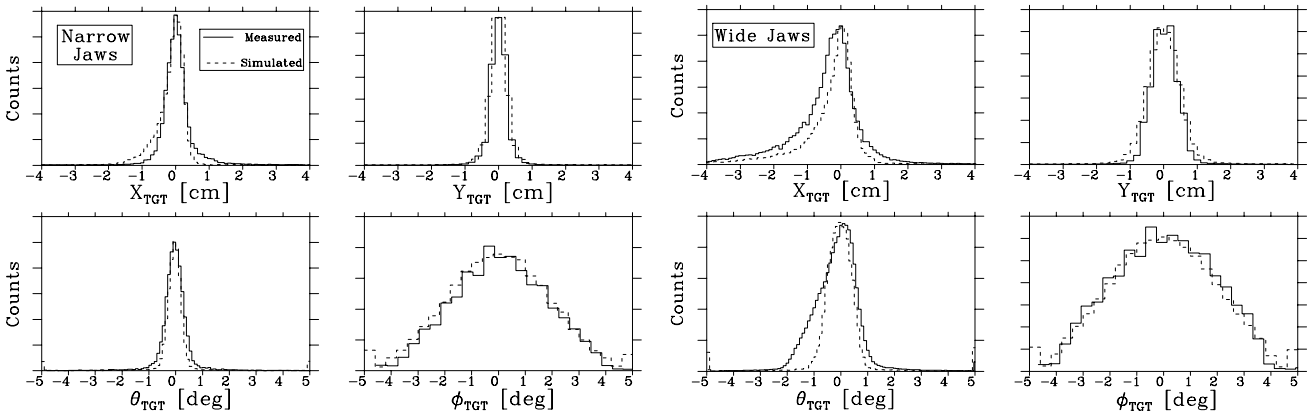

FIG. 15. Comparison of the incident pion beam size and divergence measured just prior to the experiment for two settings of the channel front–end rate–restricting jaws (*narrow*: H=50cm, V=30mm ; *wide*: H=140cm, V=120cm). Overlayed are predictions from a REVMOC simulation of the channel. The satisfying agreement lends confidence to our beam–related corrections (e.g. in–channel pion decay, Fig. 16).

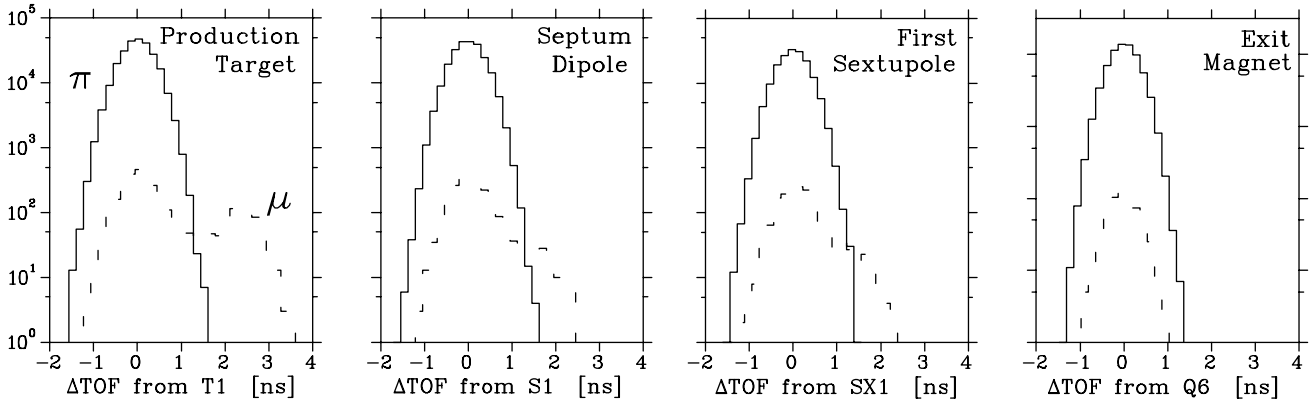

FIG. 16. REVMOC simulations of 274 MeV/c π–μ time–of–flight differences starting at different points along the pion channel. Most of the muon peak at right originates near the production target, with little contribution (≈0.2%) between the septum (first magnet after production target) and the channel exit. After the channel exit, the muon contamination under the pion peak is easily determined by REVMOC or GEANT. The number of simulated events in each spectrum is not identical.

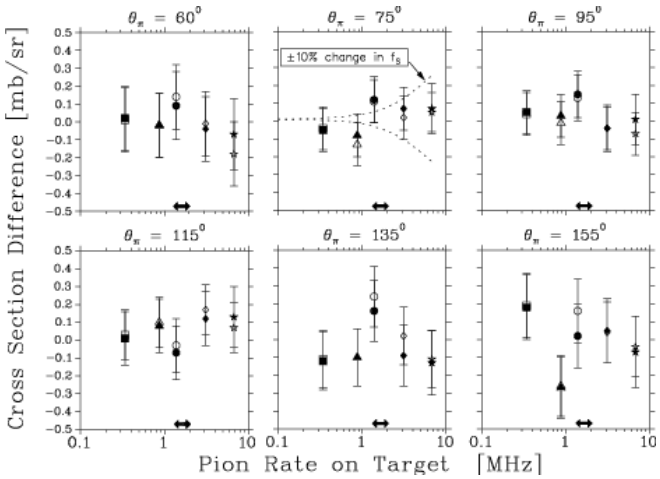

FIG. 17. π^+p cross section differences for 168.8 MeV coincidence runs using the LH_2 target, as a function of incident pion rate. The uncertainties shown are purely statistical. The independent correction methods using the VETO counter (f_S^V solid) and incident BEAM correction (f_S^P open) differed by at most 0.3% at the highest rate. The solid double arrow signifies the incident pion rate range for production runs.

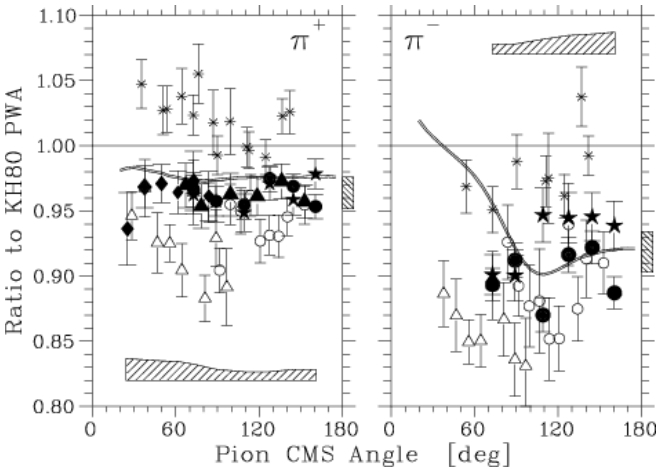

FIG. 18. Differential cross section results at 141.15 MeV (π^+p left and π^-p right) plotted as ratios to the KH80 PWA solution [17]. The solid diamond, circle, triangle, and star points represent the single–arm LH_2, two–arm LH_2 set "A" and set "B", and two–arm CH_2 results, respectively. The error bars shown are statistical only. The results of Bussey et al. [26] (asterixes) and Brack et al. [28,29] (open points) are shown as ratios to KH80 at their respective energies. The double line is the prediction of the V.P.I. SM95 PWA [19]. The horizontal hatched area represents the undertainty due to a 1σ *increase* in the beam energy, and the vertical hatched areas represent the typical $\pm 1\sigma$ normalization uncertainties for *each* of our data sets.

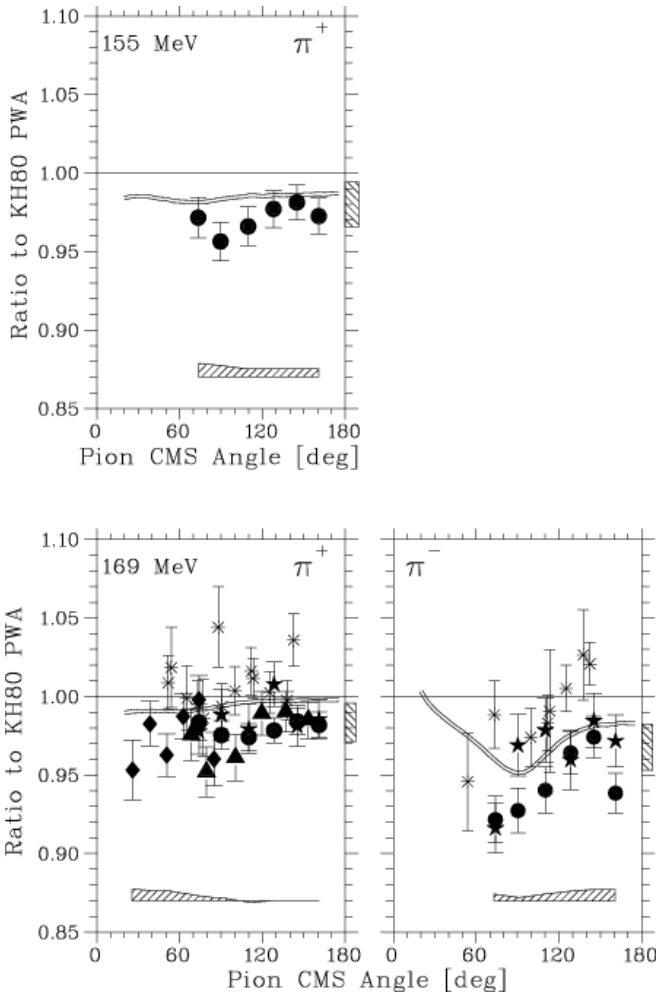

FIG. 19. As Fig 18, but showing our 154.6 MeV π^+p data (top) and our 168.8 MeV π^+p and π^-p data (bottom). Note that at 168.8 MeV, the π^+ $+1\sigma$ error band due to the energy uncertainty changes sign near 100° then stays near zero.

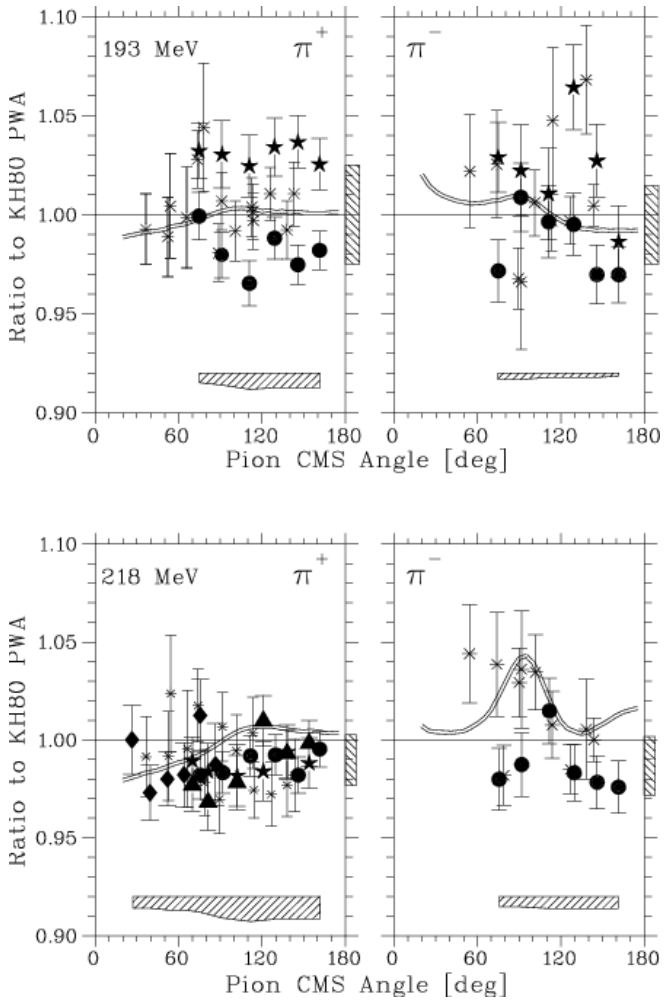

FIG. 20. As Fig. 18, but showing our 193.2 MeV π^+p and π^-p data (top) and our 218.1 MeV π^+p and π^-p data (bottom). Note that at 218.1 MeV and higher energies, the $+1\sigma$ error band due to the energy uncertainty has changed sign with respect to Fig. 18.

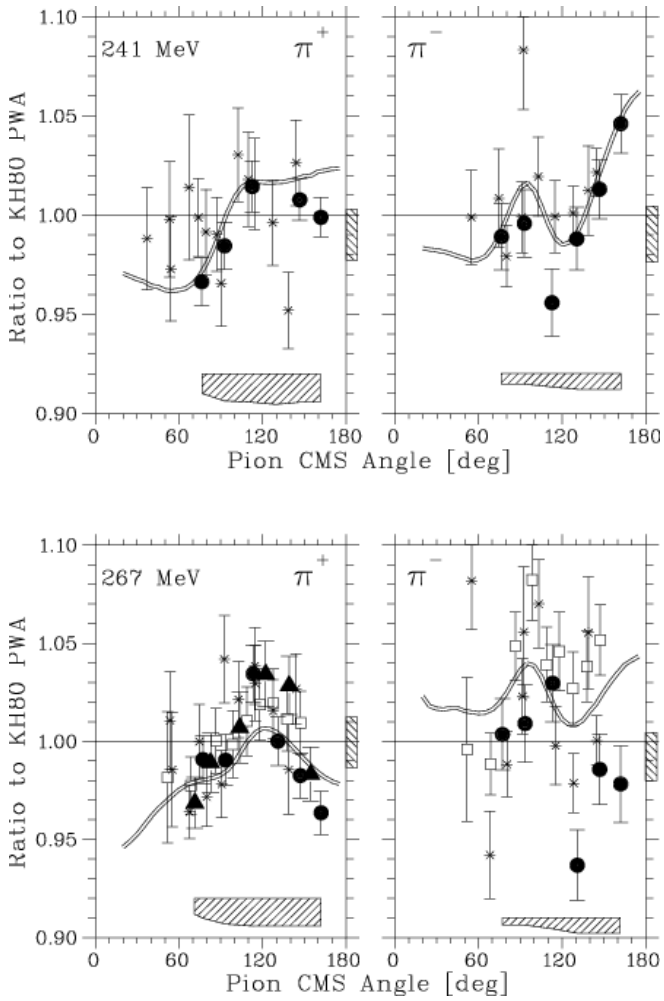

FIG. 21. As Fig. 18, but showing our 240.9 MeV π^+p and π^-p data (top) and our 267.3 MeV π^+p and π^-p data (bottom), where the LAMPF data of Sadler, et al. (263 MeV) [30] are also shown (open boxes).

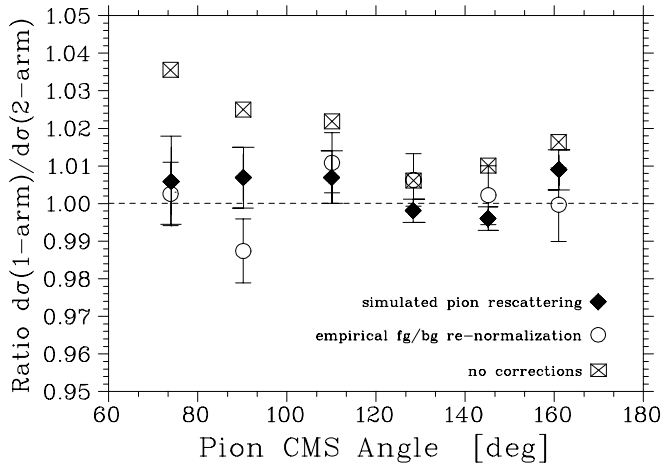

FIG. 22. Ratio of the π^+p single–arm cross section to the coincidence values at 169 MeV using the LH_2 target, for a run where the two were obtained *simultaneously*. The filled diamonds (crossed boxes) show the results where the corrections due to pion hadronic rescattering in the vacuum vessel were (were not) included in the solid angle simulations. The circles show the result using the uncorrected solid angles, where the full–/empty– target normalization was obtained by matching the backgrounds. The uncertainties reflect the 33% simulation uncertainty in the additional rescattering correction, or the uncertainties in the full/empty normalization. The corrected results verify that the rescattering correction was under control.

TABLE I. Areal densities of target nuclei for the carbon, LH_2 and CH_2 targets used in the experiment.

Target	Thickness [mg/cm^2]	H Thickness [10^{-6} mb^{-1}]
LH_2	106.2±0.5	63.43±0.32
CH_2 "A"	44.0±0.1	3.78±0.04
CH_2 "D"	185.8±0.7	16.00±0.16
CH_2 "E"	294.2±0.3	25.30±0.25
graphite	285.7	-±-

TABLE II. Normalization (i.e. scattering angle independent) and typical angle–dependent uncertainties ($100{\cdot}\sigma_X/X$) for the 168.8 MeV cross sections. All columns except the first refer to the two-arm configuration. The uncertainties at other energies are similar. The quantities in parentheses indicate final results which were obtained by averaging several runs (see text). The normalization factors are defined in equations 2 and 3.

NORMALIZATION UNCERTAINTIES (%)

	π^+p			π^-p	
Factor	1 Arm LH_2	LH_2	CH_2 "D"	LH_2	CH_2 "D"
N_{prot}	0.5	0.5	1.0	0.5	1.0
cos θ_{tgt}	0.6	1.1 (0.9)	0.6	1.1	0.6
B	<0.1	<0.1	<0.1	<0.1	<0.1
f_π	0.2	0.2	0.2	0.6	0.6
f_D	0.2	0.2	0.2	0.2	0.2
f_L	0.3	0.3	0.2	0.2	0.1
f_S	0.4	0.4 (0.1)	0.4	0.6	0.6
f_{LT}	<0.1	<0.1	<0.1	<0.1	<0.1
edge effect	0.1	0.1	0.1	0.1	0.1
$\sqrt{\sum(\Delta_i)^2}$	1.1	1.3 (1.1)	1.3	1.4	1.5

ANGLE DEPENDENT UNCERTAINTIES (%)

	π^+p			π^-p	
Source	1 Arm LH_2	LH_2	CH_2 "D"	LH_2	CH_2 "D"
Yield[a]	1.6	1.0 (0.7)	1.4 (0.8)	1.4	1.7
Solid Angle:					
MC statistics	0.4	0.4	0.4	0.4	0.4
$R_{\pi 2}$±3mm	0.5	0.5	0.5	0.5	0.5
π2 Area	0.3	0.3	0.3	0.3	0.3
hadronic losses	0.3	0.4	0.3	0.3	0.3
$\sqrt{\sum(\delta_i)^2}$	1.8	1.3 (1.0)	1.6 (1.2)	1.6	1.9

[a]including uncertainty from background subtraction

TABLE III. Centre–of–mass absolute differential cross sections at 141.15 MeV. All the stated uncertainties are at the 1σ level. The angle–dependent uncertainties and the normalization uncertainty ΔN are quadrature sums of the various contributions listed in Table II. The label Σ indicates the *linear* sum of the individual normalization uncertainties. The uncertainty in the scatering angle $\Delta\theta_{cms} = \pm 0.1^\circ$.

T_π = 141.15 ± 0.6 MeV		Absolute Differential Cross Sections [mb/sr]	
Setup	$\theta^\circ_{\rm cms}$	$\frac{d\sigma}{d\Omega}(\pi^+ p)$	$\frac{d\sigma}{d\Omega}(\pi^- p)$
		[ΔN = 1.1% (Σ = 2.3%)]	[N/A]
LH_2	25.3	15.17 ± 0.45	-
Single Arm	37.7	13.72 ± 0.23	-
	49.8	11.17 ± 0.17	-
	61.6	8.77 ± 0.15	-
	72.9	7.27 ± 0.17	-
	83.8	6.61 ± 0.13	-
		[ΔN = 1.3% (Σ = 2.7%)]	[N/A]
LH_2	67.3	7.92 ± 0.14	-
Two Arm	78.4	6.71 ± 0.12	-
	99.4	7.68 ± 0.13	-
	118.6	11.76 ± 0.18	-
	136.2	17.24 ± 0.24	-
	152.7	21.63 ± 0.29	-
		[ΔN = 1.3% (Σ = 2.6%)]	[ΔN = 1.6% (Σ = 3.4%)]
LH_2	72.9	7.22 ± 0.10	0.936 ± 0.012
Two Arm	89.1	6.69 ± 0.08	0.695 ± 0.010
	109.2	9.37 ± 0.11	0.669 ± 0.010
	127.6	14.59 ± 0.15	0.944 ± 0.014
	144.6	19.71 ± 0.19	1.247 ± 0.017
	160.7	23.26 ± 0.23	1.426 ± 0.020
		[ΔN = 1.3% (Σ = 2.6%)]	[ΔN = 1.6% (Σ = 3.4%)]
2 mm CH_2	72.9	7.19 ± 0.11	0.944 ± 0.016
Two Arm	89.1	6.69 ± 0.11	0.686 ± 0.015
	109.2	9.31 ± 0.14	0.728 ± 0.016
	127.6	14.53 ± 0.19	0.973 ± 0.020
	144.6	19.50 ± 0.24	1.279 ± 0.025
	160.7	23.87 ± 0.28	1.509 ± 0.030

TABLE IV. Centre–of–mass absolute π^+p differential cross sections at 154.6 MeV.

T_π = 154.6 ± 0.7 MeV		Absolute Differential Cross Sections [mb/sr]
Setup	$\theta^\circ_{\rm cms}$	$\frac{d\sigma}{d\Omega}(\pi^+ p)$
		[ΔN = 1.4% (Σ = 2.9%)]
LH_2	73.4	8.97 ± 0.12
Two Arm	89.6	7.81 ± 0.10
	109.6	10.74± 0.14
	128.0	16.66± 0.20
	144.9	22.88± 0.26
	160.8	27.28± 0.32

TABLE V. Centre–of–mass absolute differential cross sections at 168.8 MeV.

T_π = 168.8 ± 0.7 MeV		Absolute Differential Cross Sections [mb/sr]	
Setup	$\theta^\circ_{\rm cms}$	$\frac{d\sigma}{d\Omega}(\pi^+ p)$	$\frac{d\sigma}{d\Omega}(\pi^- p)$
		[ΔN = 1.1% (Σ = 2.5%)]	[N/A]
LH_2	25.8	25.50 ± 0.51	-
Single Arm	38.4	22.05 ± 0.32	-
	50.6	17.04 ± 0.24	-
	62.5	13.26 ± 0.19	-
	73.9	10.34 ± 0.16	-
	84.9	8.48 ± 0.15	-
		[ΔN = 1.3% (Σ = 2.7%)]	[N/A]
LH_2	68.3	11.42 ± 0.18	-
Two Arm	79.4	8.95 ± 0.15	-
	100.4	9.09 ± 0.14	-
	119.4	14.14 ± 0.20	-
	136.9	20.83 ± 0.27	-
	153.2	26.71 ± 0.33	-
		[ΔN = 1.1% (Σ = 2.3%)]	[ΔN = 1.4% (Σ = 3.1%)]
LH_2	73.9	10.19 ± 0.12	1.170 ± 0.018
Two Arm	90.2	8.46 ± 0.08	0.846 ± 0.013
	110.1	11.15 ± 0.10	0.960 ± 0.015
	128.4	17.26 ± 0.14	1.475 ± 0.021
	145.2	23.90 ± 0.19	2.069 ± 0.028
	161.0	28.82 ± 0.23	2.430 ± 0.033
		[ΔN = 1.3% (Σ = 2.6%)]	[ΔN = 1.5% (Σ = 3.2%)]
2 mm CH_2	73.9	10.13 ± 0.15	1.163 ± 0.020
Two Arm	90.2	8.57 ± 0.14	0.884 ± 0.018
	110.1	11.21 ± 0.18	0.999 ± 0.021
	128.4	17.78 ± 0.25	1.468 ± 0.029
	145.2	23.83 ± 0.32	2.091 ± 0.037
	161.0	28.93 ± 0.37	2.516 ± 0.043

TABLE VI. Centre–of–mass absolute differential cross sections at 193.15 MeV. As dicussed in Sec. IV, the normalization uncertainties were increased to 2.5% and 2.0% for π^+p and π^-p scattering, respectively, to account for the systematic difference between the CH_2 and LH_2 results at this one energy. To mimic the results at other energies, the linear sum uncertainty (Σ) was arbitrarily set to double the 1σ uncertainty.

T_π = 193.15 ± 0.7 MeV		Absolute Differential Cross Sections [mb/sr]	
Setup	$\theta^\circ_{\rm cms}$	$\frac{d\sigma}{d\Omega}(\pi^+ p)$	$\frac{d\sigma}{d\Omega}(\pi^- p)$
		[ΔN = 2.5% (Σ = 5.0%)]	[ΔN = 2.0% (Σ = 4.0%)]
LH_2	74.8	10.03 ± 0.12	1.101 ± 0.018
Two Arm	91.0	7.52 ± 0.09	0.824 ± 0.014
	110.9	9.29 ± 0.11	0.987 ± 0.018
	129.0	14.82 ± 0.16	1.581 ± 0.025
	145.7	20.43 ± 0.21	2.211 ± 0.034
	161.3	25.04 ± 0.25	2.729 ± 0.040
		[ΔN = 2.5% (Σ = 5.0%)]	[ΔN = 2.0% (Σ = 4.0%)]
2 mm CH_2	74.8	10.36 ± 0.14	1.166 ± 0.020
Two Arm	91.0	7.91 ± 0.13	0.835 ± 0.019
	110.9	9.86 ± 0.15	1.001 ± 0.023
	129.0	15.51 ± 0.22	1.691 ± 0.034
	145.7	21.73 ± 0.28	2.342 ± 0.042
	161.3	26.15 ± 0.33	2.776 ± 0.051

TABLE VII. Centre–of–mass absolute differential cross sections at 218.1 MeV.

T_π = 218.1 ± 0.8 MeV		Absolute Differential Cross Sections [mb/sr]	
Setup	$\theta^\circ_{\rm cms}$	$\frac{d\sigma}{d\Omega}(\pi^+p)$	$\frac{d\sigma}{d\Omega}(\pi^-p)$
		[ΔN = 1.2% (Σ = 2.6%)]	[N/A]
LH_2	26.5	26.16 ± 0.46	-
Single Arm	39.3	20.58 ± 0.30	-
	51.8	15.75 ± 0.22	-
	63.9	11.38 ± 0.19	-
	75.4	8.29 ± 0.15	-
	86.4	6.11 ± 0.13	-
		[ΔN = 1.3% (Σ = 2.6%)	[ΔN = 1.5% (Σ = 3.0%)
LH_2	75.6	8.04 ± 0.10	0.923 ± 0.015
Two Arm	91.9	5.62 ± 0.06	0.663 ± 0.011
	111.8	6.72 ± 0.07	0.847 ± 0.014
	129.7	10.59 ± 0.11	1.353 ± 0.020
	146.2	14.85 ± 0.14	1.948 ± 0.027
	161.5	18.41 ± 0.17	2.395 ± 0.033
		[ΔN = 1.3% (Σ = 2.8%)]	[N/A]
LH_2	69.9	9.49 ± 0.13	-
Two Arm	81.2	6.78 ± 0.10	-
	102.1	5.60 ± 0.08	-
	121.0	8.62 ± 0.11	-
	138.1	12.86 ± 0.16	-
	154.0	16.98 ± 0.20	-
		[ΔN = 1.5% (Σ = 3.1%)]	[N/A]
3.2 mm CH_2	69.9	9.61 ± 0.12	-
Two Arm	81.2	6.886 ± 0.095	-
	102.1	5.621 ± 0.090	-
	121.0	8.40 ± 0.13	-
	138.1	12.87 ± 0.18	-
	154.0	16.81 ± 0.22	-

TABLE VIII. Centre–of–mass absolute differential cross sections at 240.9 MeV. The π^+ point at 130.3^0 has been deleted since the proton counter for this run was found to be seriously misaligned.

T_π = 240.9 ± 0.9 MeV		Absolute Differential Cross Sections [mb/sr]	
Setup	$\theta^\circ_{\rm cms}$	$\frac{d\sigma}{d\Omega}(\pi^+p)$	$\frac{d\sigma}{d\Omega}(\pi^-p)$
		[ΔN = 1.3% (Σ = 2.8%)]	[ΔN = 1.4% (Σ = 2.9%)]
LH_2	76.3	6.35 ± 0.08	0.822 ± 0.013
Two Arm	92.7	4.08 ± 0.05	0.585 ± 0.010
	112.5	4.68 ± 0.06	0.675 ± 0.012
	130.3	- ± -	1.127 ± 0.018
	146.6	10.65 ± 0.11	1.634 ± 0.024
	161.8	12.93 ± 0.13	2.046 ± 0.029

TABLE IX. Centre–of–mass absolute differential cross sections at 267.3 MeV.

T_π = 267.3 ± 0.9 MeV		Absolute Differential Cross Sections [mb/sr]	
Setup	$\theta^\circ_{\rm cms}$	$\frac{d\sigma}{d\Omega}(\pi^+ p)$	$\frac{d\sigma}{d\Omega}(\pi^- p)$
		[ΔN = 1.3% (Σ = 2.7%)]	[ΔN = 1.2% (Σ = 2.5%)]
LH_2	77.2	4.773 ± 0.057	0.718 ± 0.011
Two Arm	93.5	2.793 ± 0.036	0.508 ± 0.010
	113.3	3.025 ± 0.041	0.575 ± 0.011
	131.0	4.812 ± 0.059	0.835 ± 0.016
	147.1	6.959 ± 0.081	1.263 ± 0.023
	162.1	8.526 ± 0.098	1.542 ± 0.031
		[ΔN = 1.3% (Σ = 2.8%)]	[N/A]
LH_2	71.4	5.779 ± 0.075	-
Two Arm	82.8	3.875 ± 0.058	-
	103.7	2.565 ± 0.045	-
	122.3	3.862 ± 0.062	-
	139.2	6.134 ± 0.088	-
	154.7	7.93 ± 0.11	-